The Ocean Color Instrument (OCI) on the Plankton, Aerosol, Cloud, ocean Ecosystem (PACE) Mission: System Design and Prelaunch Radiometric Performance

Gerhard Meister, Joseph J. Knuble, Ulrik Gliese, Robert Bousquet, Leland H. Chemerys, Hyeungu Choi, Robert E. Eplee, Robert H. Estep Jr., Eric T. Gorman, Samuel Kitchen-McKinley, David Kubalak, Shihyan Lee, Charles McClain, Jeffrey W. McIntire, Frederick S. Patt, Zakk Rhodes, and P. Jeremy Werdell

***Abstract*— The Ocean Color Instrument (OCI) is the primary payload on NASA's Plankton, Aerosol, Cloud, ocean Ecosystem (PACE) mission. Its primary purpose is to enable new scientific studies of ocean biology, aerosols, and clouds. This article describes the design of the instrument and its radiometric performance as measured during the prelaunch characterization campaign. OCI will be the first radiometer to provide hyperspectral (340–895 nm) daily global coverage of top-of-atmosphere (TOA) radiances. Seven multispectral bands cover wavelengths from 940 to 2260 nm. The spatial resolution is about 1.2 km. OCI performance is optimized for ocean color applications, with a focus on high signal-to-noise ratio (SNR) at low radiance levels and high radiometric accuracy.**

***Index Terms*— Calibration, hyperspectral sensors, remote sensing.**

I. Introduction

NASA's Plankton, Aerosol, Cloud, ocean Ecosystem (PACE) mission [1] launched on February 8, 2024. Its primary payload is the Ocean Color Instrument (OCI). OCI will provide global top-of-atmosphere (TOA) radiance measurements to support ocean color [2], [3], [4], aerosol [5], and cloud studies [6], [7]. OCI significantly improves the spectral coverage below 2260-nm relative to previous global TOA radiance sensors, such as SeaWiFS [8], moderate resolution imaging spectroradiometer (MODIS) [9], medium resolution imaging spectrometer (MERIS) [10], ocean and land colour instrument (OLCI) [11], and visible infrared imaging radiometer suite (VIIRS) [12]. From 340 to 895 nm, it provides hyperspectral coverage (5-nm bandwidth, with either 2.5- or 1.25-nm sampling, i.e., overlapping bands), and multispectral coverage (seven discrete wavelengths) from 940 to 2260 nm. Although its spatial resolution is only about 1.2 km (further increasing toward the edge of the scan), its unique spectral and global coverage is expected to be useful for other disciplines (e.g., land remote sensing) as well. Combining OCI data with data from the two multiangle polarimeters (Hyper Angular Research Polarimeter 2 (HARP-2) [13] and Spectro-polarimeter for Planetary Exploration (SPEXone) [14]) on-board the PACE spacecraft will provide additional new application possibilities (see [15], [16]). A detailed overview of the science goals of the PACE mission has been provided by Werdell et al. [1].

PACE will orbit the Earth in a sun-synchronous polar orbit with an equatorial local crossing time of 13:00 at an altitude of 676.5 km. OCI will be tilted by 20° in the track direction away from the sun to avoid glint from the ocean surface. The OCI tilt maneuver will occur every orbit close to the subsolar point. Its location will be staggered from day-to-day relative to the optimal location [17] to reduce consistent coverage gaps in the equatorial region. OCI will map more than 95% of the sunlit Earth daily.

OCI has a long development history, starting in 2000 with a NASA study on what future satellite observations are required for carbon cycle research [18]. The Ocean Radiometer for Carbon Assessment (ORCA) was built as a laboratory demonstration unit starting in 2008 [19], [20], [21], demonstrating many of the critical design concepts used in OCI. The development of ORCA included specification of ocean color instrument performance requirements [22] that were

Manuscript received 21 February 2024; revised 21 March 2024; accepted 23 March 2024. Date of publication 1 April 2024; date of current version 13 May 2024. This work was supported by the Plankton, Aerosol, Cloud, ocean Ecosystem (PACE) project of the National Aeronautics and Space Administration (NASA). *(Corresponding author: Gerhard Meister.)*

Gerhard Meister, Joseph J. Knuble, Robert H. Estep Jr., David Kubalak, and P. Jeremy Werdell are with NASA, Goddard Space Flight Center, Greenbelt, MD 20771 USA (e-mail: gerhard.meister@nasa.gov; joseph.j.knuble@nasa.gov; robert.h.estep@nasa.gov; david.kubalak@nasa.gov; jeremy.werdell@nasa.gov).

Ulrik Gliese is with KBR, Fulton, MD 20759 USA (e-mail: ulrik.b.gliese@nasa.gov).

Robert Bousquet is with Genesis Engineering Solutions Inc., Lanham, MD 20706 USA (e-mail: robert.r.bousquet@nasa.gov).

Leland H. Chemerys, Samuel Kitchen-McKinley, and Jeffrey W. McIntire are with Science Systems and Applications Inc., Lanham, MD 20706 USA (e-mail: leland.h.chemerys@nasa.gov; samuel.kitchen@ssaihq.com; jeffrey.mcintire@ssaihq.com).

Hyeungu Choi is with Global Science & Technology Inc., Greenbelt, MD 20707 USA (e-mail: HChoi@gst.com).

Robert E. Eplee, Shihyan Lee, and Frederick S. Patt are with Science Applications International Corporation, Reston, VA 20190 USA (e-mail: robert.e.eplee@nasa.gov; shihyan.lee@nasa.gov; frederick.s.patt@nasa.gov).

Eric T. Gorman is with Northrop Grumman, Baltimore, MD 21240 USA (e-mail: eric.gorman@quantumspace.us).

Charles McClain, retired, was with NASA, Goddard Space Flight Center, Greenbelt, MD 20771 USA. He is now with Severna Park, MD 21146 USA (e-mail: chuckmcclain@verizon.net).

Zakk Rhodes is with the Space Dynamics Laboratory, UT 84341 USA (e-mail: zakk.rhodes@nasa.gov).

Digital Object Identifier 10.1109/TGRS.2024.3383812

largely applied to the OCI. The PACE Science Definition Team was established in 2011. The team provided a revised set of the OCI performance requirements [23] to NASA. The OCI characteristics discussed in this introduction meet all the Science Definition Team OCI threshold requirements and several of the additional goal requirements. The final OCI requirements were established by the PACE mission with a newly introduced "design-to-cost" approach [1].

NASA Headquarters assigned the PACE mission to the Goddard Space Flight Center (GSFC) in December 2014. The two polarimeters (SPEXone and HARP2) were provided by a partnership of Space Research Organization of the Netherlands (SRON) and Airbus Defense and Space Netherlands, and the University of Maryland, Baltimore County, respectively. OCI was designed, built, and tested at GSFC. As the name implies, its primary objective is to support ocean color research. Ocean color measurements require a very high degree of relative accuracy [24]. Absolute accuracy is secondary [25] because for most bands, absolute calibration is adjusted via vicarious calibration [26]. Therefore, a comprehensive prelaunch radiometric calibration campaign characterizing all error sources was a critical part of the OCI development. Most of the radiometric characterization measurements were performed both for the OCI flight unit and the OCI Engineering Test Unit (ETU), allowing the OCI Team to apply lessons learned from the ETU campaign [27] to the flight unit characterization.

The OCI flight unit instrument level characterization lasted for 6 months, from April to October 2022, including a 2-month thermal vacuum campaign (TVAC) [28]. Additional OCI tests at the PACE observatory level concluded in August 2023, including another 2-month TVAC campaign.

This article consists of two main parts: 1) a description of the design of the instrument, with subsections for each subsystem and 2) measured instrument performance parameters, focusing on spectral characteristics, absolute calibration, signal-to-noise ratio (SNR), response versus scan angle (RVS), polarization, linearity, response to temperature variations, stray light, and spatial characteristics. Papers that provide more background information dedicated to specific performance parameters and how they were measured are referenced, or will be published at a later date.

II. OCI System Design

A. OCI Image Acquisition

OCI uses the PACE spacecraft motion to image the Earth along the spacecraft track. OCI has a rotating telescope that provides cross track scans at a frequency of 5.77 Hz. The telescope rotation speed is chosen such that the along track progression of OCI along its orbit results in along track sampling of 1 km on the ground for nadir pointing. Detector measurements are recorded at (see Fig. 1):

1) a range of ±56° around nadir (Earth view data);
2) −90° (solar calibration assembly (SCA), see Section II-H);
3) +90° solar pulse calibration assembly (SPCA), see Section II-I);

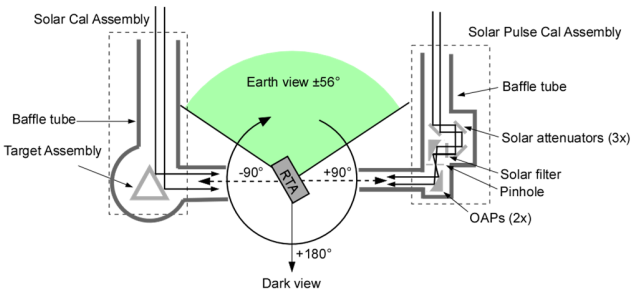

Fig. 1. OCI telescope scan diagram: RTA, SCA, and SPCA (OAP—off-axis parabolic mirror).

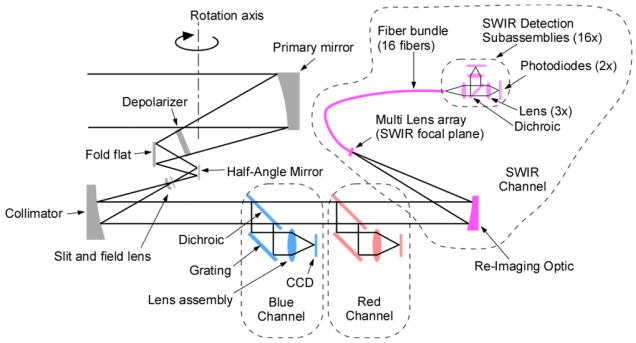

Fig. 2. OCI optical path. Light enters the primary mirror from the left in the diagram.

4) +180° [scan cavity, for dark current subtraction, see Section III, (1)].

The rotating telescope directs the incoming light to a half-angle mirror (HAM) that rotates at half the speed of the telescope, thereby maintaining a stationary optical path thereafter. From there, the light is directed to one of three channels (blue, red, and short-wave infrared (SWIR), see Fig. 2). Gratings disperse the light to charge-coupled devices (CCDs) in the Blue and Red channels. The CCDs capture the light with 512 pixels in the spectral dimension and 128 pixels in the spatial dimension. The SWIR bands use photodiodes with spectral bandpass filters, see Fig. 2.

The high rotation speed of the telescope results in a small integration time for individual CCD pixels, leading to a small SNR per CCD pixel. OCI uses on-chip time-delay-integration (TDI, see [20]) to improve SNR, as did sea-viewing wide field-of-view sensor (SeaWiFS). Basically, light striking each detector on the CCD array induces a charge, which is transferred and accumulated down array to the readout register, at a speed synchronized with the rotating telescope such that each ground pixel is viewed multiple times, thereby increasing the SNR of the integrated value. The instantaneous field of view (IFOV) of OCI corresponds approximately to an area on the ground of 1 km in track direction times 16 km in the scan direction, determined by the slit. Each pixel on the CCD images an area with a width of 125 m in the scan direction, with an integration time of 5.4 μs. The CCDs perform an analog 128:1 TDI via charge transfer. Eight adjacent 125-m pixels in scan direction are aggregated digitally on-board (see Section II-E) to 1-km "science pixels," in order to reduce the data rate. This means that for each spectral band (without spectral aggregation), the charge from 128 CCD pixels is accumulated for each 125-m pixel, and eight of these pixels are integrated into a 1-km Science Pixel that contains

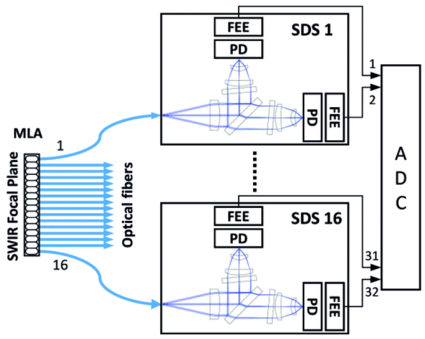

Fig. 3. SWIR detection system. Only two of the 16 SWIR SDSs are shown. PD—photodiode. Figure taken from [30].

TABLE I

POSITIONING OF THE SWIR BAND FIBERS IN THE MLA. DURING IMAGE ACQUISITION, THE IMAGE MOVES FROM POSITION 16 TO POSITION 1. THE BANDS AT MLA POSITIONS 3 AND 4 ARE STANDARD GAIN, 5–12 ARE HIGH GAIN

MLA POSITION	BAND 1	BAND 2
1-2	940NM	1378NM
3-12	1250NM	1615NM
13-14	1038NM	2130NM
15-16	1038NM	2260NM

1024 times the charge of a single CCD pixel. For a spectral aggregation of eight spectral pixels (the product provided to the science users), a 1-km Science Pixel contains the charge from 8192 CCD pixels.

Whereas each hyperspectral band views the whole 16-km wide OCI IFOV at any moment in time, an individual SWIR band only view parts of the OCI IFOV, depending on its position in the multilens array (MLA), see Fig. 3 and Table I. Each of the 16 MLA lenses (and its two associated SWIR detectors) images an area with a width in scan (and track) direction of ∼1 km. The number of detectors per band varies from 2 to 8, depending on the SNR goal of the SWIR band. To further improve SNR at low radiance levels, light at 1250 and 1615 nm is acquired via high gain bands in addition to the standard gain bands. The two high gain bands (with 8:1 digital TDI) saturate below typical cloud radiances, while the two standard gain bands (with 2:1 digital TDI) cover the whole dynamic range up to maximum cloud radiances. The 1038-nm band is optimized for low to medium radiance levels with a digital TDI of 4:1, and saturates below maximum cloud radiances, see Section III-G.

B. Optical Path

The optical path from the telescope to the detectors is shown in Fig. 2. The rotating telescope contains three optical elements: the primary mirror, fold flat, and depolarizer. Light enters the optical system through a 340-mm-long baffled tube. The first element in the telescope is the primary mirror, an off-axis parabolic (OAP) mirror that focuses the light down toward a slit later in the optical path. A mask on the primary mirror is the entrance pupil and aperture stop of the system. The primary has a UV-enhanced broadband reflective silver coating similar to the coating developed for ORCA, see [29]. After leaving the primary mirror, the light passes through the depolarizer, an uncoated double-wedge MgF2 polarization scrambler. The two wedges have their crystal axes clocked 45° with respect to each other. Finally, the light path is folded by the fold flat mirror before leaving the telescope assembly.

The next optical element is the HAM. The HAM is a double-sided flat mirror rotating at half the speed of the telescope. Rotating at half-speed cancels the effect of the rotating telescope, leading to a stationary light path. Because of this half-speed rotation, both sides of the HAM are used, alternating with each rotation of the telescope. The same UV-enhanced silver coating is used on both sides of the HAM. It is critical to match the coating performance of the two sides to avoid scan-line striping in the image.

Light leaving the HAM is focused onto a stationary knife-edge slit. The slit is the field stop of the system, defining the 1 × 16 science pixels on the ground. Immediately after the slit is a weak field lens and collimator mirror. The collimator recollimates the light to enable a split into three channels. The weak field lens pushes the virtual pupil formed by the primary and collimator mirrors out to the gratings, so that the spectral and spatial pupils are in the same plane.

Light is split into three channels using two dichroics. Light below 600 nm is reflected into the blue channel, while 600–900 nm is reflected into the red channel. Since no dichroic cutoff is perfect, a small transition region around 600 nm is imaged into both channels. Wavelengths longer than 900 nm are allowed to pass to the SWIR channel. Attenuators are placed between the red dichroic and the red grating (single blade design) and between the red dichroic and the reimaging optics (RIO) (double blade design) to avoid saturation, see Section III-G.

Each of the blue and red hyperspectral channels has a grating optimized for the wavelengths of that channel, and a lens assembly that focuses the wavelength-dispersed slit image onto a CCD. The lens assemblies were especially difficult to design and build due to their wide range of wavelengths and field angles, low f/number, and space constraints. Fortunately, coatings used in each channel can be optimized for a smaller range. The hyperspectral detector systems are described further in Section II-C.

The first element in the SWIR channel is the RIO, which is another OAP that refocuses the slit image onto the MLA. The MLA and SWIR detector subassemblies are described further in Section II-D. Additional details on the OCI optical path are provided in [30].

C. Hyperspectral Detectors and Read-Out Electronics

The ultraviolet (UV) to near-infrared (UVNIR) optoelectronic detection system [30] consists of a UV to visible (VIS) focal plane assembly (FPA, "blue") and a VIS to NIR FPA ("red"), each containing the following.

1) A 128 × 512 pixel Si CCD with 16 readout channels ("taps") of 32 columns per channel operated in on-chip analog charge transfer TDI mode. Each column corresponds to a spectral band, so each tap has 32 spectral bands, and each CCD provides 512 spectral bands.
2) A 16-channel front-end electronics (FEE) board with dc clamps, amplifiers, noise filters, and two fast,

low-power eight-channel 14-bit analog-to-digital converters (ADCs).

3) A thermal system to allow efficient cooling of the CCD and FEE while ensuring excellent mechanical alignment to the FPA housing with high thermal isolation.

To achieve the required OCI spatial and spectral resolution, the CCDs have to be operated at a high read-speed making it challenging to simultaneously achieve the low noise and high precision required for OCI. At the OCI telescope scan rate, it takes a 1-km ground scene 43 μs to move one Science Pixel in the detection system (integration time). Since each CCD pixel corresponds to a 125-m ground scene, a CCD image area pixel must complete charge integration, transfer of charge, and readout in 5.4 μs. It is necessary to read the charge of all 32 image area pixels of a tap in those 5.4 μs. For each read cycle, the charge is first moved from image pixel to image pixel or from image pixel to readout pixel. This parallel charge transfer is done in 940.8 ns. Then, charge is swiftly moved through the serial output pixel register to the CCD readout circuit. Each serial charge transfer is done in 117.6 ns. With four pre-read, 32 read and two postread pixels per tap, the one parallel and 38 serial transfers add up to 5.4 μs, which is the integration time for the 125-m ground scene.

The FPAs are operated with correlated double sampling (CDS), where an ADC sample is made both during the CCD reset state and the CCD video state to effectively remove the CCD reset noise. For each serial readout, the CCD is first reset, and then, the charge from the last pixel in the serial register is transferred to the sense node. Therefore, the reset and the charge transfer to the sense node must each happen and get sampled by the ADC in 58.8 ns (half of 117.6 ns). It is challenging for the CCD two-stage field effect transistor (FET) source-follower readout circuit to settle in this timeframe. A three-stage output circuit would enable faster settling time but would produce too high noise. Despite this, high read precision has been achieved by ensuring low CCD clock jitter and very stable CCD bias.

A high-modulation transfer function (MTF) and low out-of-band response ratio require high charge transfer efficiency (CTE) and low readout channel-to-channel crosstalk in the CCDs. They are implemented with high CTE as well as high output channel density to reduce read speed as much as possible in trade-off with crosstalk. In addition, due to the requirement of detection of ocean and cloud signals with no gain change, the system must have a high dynamic range. This requires a large CCD well and sense node capacity of $\geq$750 ke- together with a 14-bit ADC.

An outstanding performance has been achieved for this system despite challenging and conflicting requirements [30].

D. SWIR Detectors and Read-Out Electronics

The seven-band 940–2260-nm shortwave infrared (SWIR) optoelectronic detection system [30], [31] consists of a focal plane in the form of a 16 $\times$ 1 MLA, where each lens corresponds to a 1 $\times$ 1 km Science Pixel on the ground. The MLA is fiber coupled to 16 SWIR detection subassemblies (SDSs), as shown in Fig. 3. Each SDS contains optics splitting the input out to two spectral bandpass filters (see Table I) that are each followed by a photodiode and an FEE feeding analog signals into a multichannel 16-bit ADC. Varying amounts of the 32 photodiodes are assigned to each of the seven bands (see Table I), digital TDI is applied after detection. InGaAs photodiodes are used below 1400 nm, and HgCdTe photodiodes are above 1600 nm.

Achieving low leakage between the lens elements in the MLA is important for accurate spatial sampling (as defined by the MTF requirements, see Section III-I), requiring the development of special fabrication techniques for the MLA. Electronically, this is a very different system than the UVNIR system. This system uses direct photo detection of each 1-km science pixel, so the integration time is high at 43 μs. This leads to a 23.3-kHz readout/sampling rate in contrast to the 17-MHz rate of the UVNIR system. However, the high cloud radiance levels and SNR requirements at low ocean radiance levels demand a high dynamic range and low noise. This requires a large area photodiode (290-μm diameter), very high gain, 16-bit ADC, and a narrow signal bandwidth. In contrast, high MTF and precision require a wide signal bandwidth and a fast pulse response. Careful design was needed to achieve a stable circuit capable of high gain with a wide enough signal bandwidth [30]. Furthermore, detailed modeling was done to optimize the bandwidth for the best possible trade between noise and MTF. A fast pulse response was not achieved due to a long-tail pulse response of the photodiodes (hysteresis) and limitations of the FEE design [31]. The effect is mitigated by the development of an in-flight pulse response measurement system (see Section II-I) and a postprocessing correction (see Section III-K) [31].

E. Data Acquisition Unit (DAU)

The DAU provides bias and clocking to the FPAs, acquires digital data from the FPAs and performs data processing in the form of CDS and digital aggregation. The DAU also synchronizes with the telescope motor controller to ensure the ground scene scan is locked to the TDI charge movement. In addition, the DAU controls the scan angle ranges (see Fig. 1) over which data are acquired.

The DAU receives the 14-bit digitized output of each CCD as a series of 512 $\times$ 128 arrays. In regular science modes, the processing of one edge tap of each CCD is disabled, reducing the number of available spectral pixels from 512 to 480. For each tap, the spatial and spectral aggregation can be chosen individually, with possible aggregations of 1, 2, 4, or 8 pixels. In "baseline" science mode, eight spatial pixels are aggregated for all taps, and the spectral aggregation is either 2 or 4. The "diagnostic" mode has no aggregation for the hyperspectral bands, resulting in a huge data rate. The data rate for this mode is reduced by providing Earth view data only over a scan angle range of 4.5°. Table II provides on overview of the most important OCI data acquisition modes.

The SWIR band data arrives at the DAU in arrays of 32 values. The 32 values are combined via digital TDI in the DAU into seven spectral bands. Special modes are available to obtain subsets of SWIR data without TDI for evaluating the performance of individual photodiodes.

TABLE II
OCI DATA MODES. SPATIAL AGGREGATION OF EIGHT AND TDI UNLESS OTHERWISE NOTED

Mode	Purpose	Description
Baseline	Global science data acquisition	Earth view data and dark view data, see Fig. 1. Spectral sampling at 2.5nm from 315nm to 895nm, with 1.25nm spectral sampling from a) 640nm-715nm and b) 740nm-775nm.
Threshold	Global science data acquisition	Same as baseline, but with spectral sampling at 5nm to reduce data volume (60 bands per CCD).
Spectral	Spectral calibration	No spectral aggregation, 32° scan angle range.
Bright Solar Diffuser	Gain/spectral Calibration	No spectral aggregation, 16° scan angle range at -90°.
SPCA	SWIR pulse response monitoring	Spectral aggregation of 8, 66° scan angle range starting at +90°.
Lunar Sweep	Lunar irradiance measurement	Same as baseline, 8° scan angle range, 125m spatial resolution.
Lunar Stare	Hysteresis monitoring	Same as threshold, 66° scan angle range.
Progressive TDI	Linearity monitoring	Progressively delayed charge transfer in CCD, see sections III.E and III.L
Time Delay	IFOV characterization	Subpixel delay of data acquisition within scan, see section III.I. Variable aggregation.
SWIR High Speed	SDS characterization	No TDI for SWIR, band subsampling.
SWIR Single Image Raw	SDS characterization	No TDI for SWIR, spatial subsampling.
Diagnostic	General testing	No spatial or spectral aggregation, 4.5° scan angle range.
Snapshot	Evaluation of individual CCD pixels	No spatial or spectral aggregation, no TDI, telescope stationary.
Raw	CCD reset and video readout performance	Raw CCD reset and video ADC samples, one CCD at a time; no Correlated Double Sampling (CDS).
Scope	CCD readout waveform performance	Raw CCD ADC samples with ADC clock aliasing in relation to CCD readout clock.

The SWIR data are always provided as 20-bit values, without truncation. The DAU truncates the blue and red FPA aggregated data from 18 to 20 bit (depending on the aggregation mode) to 16 bit.

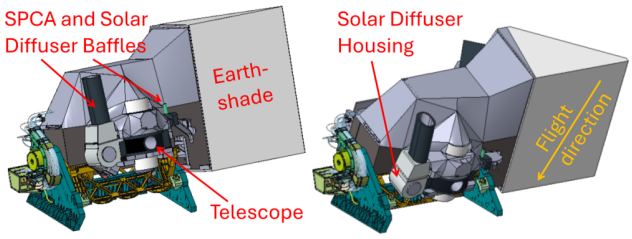

Fig. 4. OCI on the tilt mechanism (colored teal in the schematic) with tilt angle (left) −20° and (right) +20° (toward the spacecraft flight direction, shown as an orange arrow). OCI and tilt system are attached to the PACE spacecraft in an antiram configuration.

1) In the threshold mode, the four least significant bits are truncated in the Earth view range.
2) In the baseline mode, the three least significant bits are truncated in the Earth view range for taps with spectral aggregation of four (2.5-nm sampling) or the two least significant bits for taps with spectral aggregation of 2 (1.25-nm sampling).
3) The 16 least significant bits are kept in any aggregation mode in the dark view range.
4) No truncation in diagnostic mode.

For spectral aggregation of less than 8, the equivalent of eight neighboring spectral pixels (e.g., two values that each resulted from aggregating four spectral pixels in the DAU) will be summed during ground processing when converting Level 1A data (reformatted raw data from the DAU; see [32] for data level definitions) to Level 1B data (calibrated radiances or reflectances). Note that Level 1B data are provided as 16-bit floating point values for all spectral bands.

F. Structure, Bearings, and Tilt

The OCI optical system, detector systems, electronics boxes, star tracker, and Earth-shade are attached to a composite honeycomb frame. The Earth-shade (shown in Fig. 4) protects the OCI radiators from radiation coming from the Earth.

The tilt system tilts OCI ±20° (see Fig. 4) within 50 s every orbit: into the spacecraft flight direction during the sunlit side of the orbit (close to the equator), opposite to the flight direction during the dark side of the orbit. Only power and digital data pass over the tilt interface.

OCI by itself (without tilt mechanism, including the Earth shade) has a height of 1.3 m, a length of 1.3 m, and a width of 2.3 m. The OCI mass is 272 kg. For a typical orbit, OCI uses an average power of 236.5 W, provided by the solar panels of the spacecraft.

The rotating telescope mechanism and the HAM mechanism are phase locked [33]. The RT/HAM bearing is a custom superduplex hybrid bearing pair using 440C stainless steel bearing races, silicon nitride balls, and Nye Synthetic Oil 2001. The 60-lb preload on the bearing is achieved through a grinded C-spacer.

G. Thermal Control

OCI has a passive design with straps and radiators to conduct heat either to the radiators or directly to space,

with the exception of the UVNIR FPA thermal control, which requires dedicated loop heat pipes [34]. High-efficiency graphite thermal straps inside the FPAs and loop heat pipes between the FPAs and the passive radiators efficiently cool the CCDs and FEEs to cold operating temperatures and hold the system thermally stable.

Reducing temperature variations was an important design consideration, because characterizing radiometric sensitivity to temperature variations is very challenging, due to the difficulties in simulating the on-orbit temperature environment during prelaunch testing. There are a total of 23 heaters on OCI, including 15 survival heaters (needed if the spacecraft goes into safehold mode). The 74 temperature sensors are placed at various locations throughout OCI. A diagram of the thermal control system is provided in [35].

The OCI on-orbit instrument temperatures have at this moment only been modeled to within a range of about 5 °C, but the thermal control design will limit the on-orbit instrument temperature variations around the mean temperatures to ±0.5 °C on the FPAs, and ±1 °C to ±2.5 °C everywhere else. For low noise and high precision performance, the CCD and SWIR detectors are maintained at optimum temperatures for each. The detectors are the coldest areas on OCI: the SWIR detectors at approximately −65 °C, and the CCDs at approximately −25 °C. They have separate radiators, with sizes of 0.45 and 0.22 m^2, respectively. All FEEs are kept at −25 °C. The expected on-orbit temperature of the entire optical system is about +16 °C.

The HgCdTe SWIR bands need to be cooled to avoid saturation from dark current, whereas the InGaAs SWIR bands provide accurate data without cooling.

Although noise is reduced somewhat, the CCDs are primarily held at cold temperatures in order to minimize the effects of on-orbit radiation.

H. Solar Calibration Assembly (SCA)

The SCA contains a target assembly (“carousel”) with three reflective targets that are viewed by the rotating telescope assembly (RTA), see Fig. 1. One target at a time is selected with a mechanism. A door is included to limit UV exposure of the targets outside of calibration activities. Two of the targets (“bright diffusers”) are identical quasi-volume diffusers (QVDs), with one being used monthly to track possible reflectance degradation over time against the daily diffuser, similar to the approach used for MERIS [36]. The third target (“dim diffuser”) is an aluminum substrate coated with Fractal Black [37] with low reflectivity (see Fig. 5) and is used to support linearity monitoring, see Section III-L. Stray light from the Earth and spacecraft is limited by a baffle tube (see Fig. 1) to ensure that the sun is the only source of light that is observed during calibration collections.

The bidirectional reflectance function (BRDF) of the bright diffusers was measured at TNO (Delft, The Netherlands), with uncertainties ranging from 0.5% to 1.2%. Validation measurements at GSFC showed agreement within the combined uncertainties (better than 2%). The reflectance of the QVDs was spatially less homogeneous than expected: the reflectance

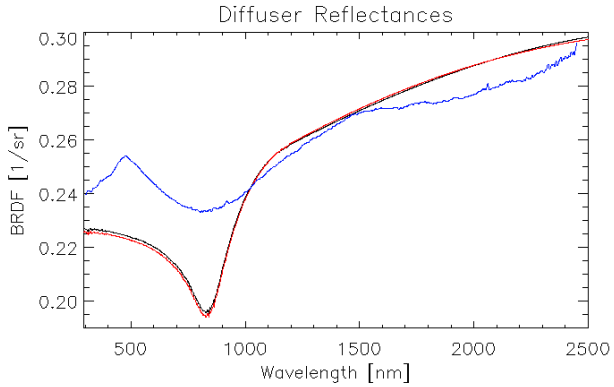

Fig. 5. BRDF of a) daily bright diffuser (black solid line), b) monthly bright diffuser (red solid line), and c) dim diffuser (blue line, multiplied by ten for plotting purposes). The BRDF of the dim diffuser varies from 0.0233 to 0.0296 sr^{-1}. The BRDF of an ideal white Lambertian diffuser is 0.318 sr^{-1}.

of the surface decreased toward its edge by several percent. The BRDF measurement plan was expanded to characterize this effect. The BRDF values for typical on-orbit angles ranged from about 0.2–0.3 sr^{-1} (minimum around 830–840 nm, increasing throughout the SWIR), see Fig. 5. The BRDF of the daily bright diffuser is about 0.5% higher than the monthly below 900 nm. A comprehensive publication on the bright diffuser BRDF measurements will be provided at a later date.

I. Solar Pulse Calibration Assembly (SPCA)

The SPCA [31] is a late addition to the OCI design, necessitated by the discovery of significant hysteresis in the SWIR bands, see Section III-K. Its purpose is to provide a sharp radiance gradient (impulse response) for monitoring hysteresis on-orbit. The optical design is shown in Fig. 1. A beam of sun light is directed via reflections to the RTA. The solar attenuators hardly transmit any light below 850 nm, but the SWIR bands are illuminated at high radiance levels without saturating the detectors. The baffle tubes of the SPCA and the SCA are pointing in the same direction, so that SPCA measurements can be acquired immediately following the SCA data acquisition, avoiding a dedicated spacecraft maneuver.

J. Instrument Command and Data Unit (ICDU)

The ICDU is built on the Modular Unified Space Technology Avionics for Next Generation (MUSTANG) architecture [38] and is the interface between the instrument and the spacecraft. It controls power switching and commanding to the different instrument components, including the heaters distributed throughout the instrument, and it reads many of the OCI temperature sensors. The ICDU is composed of six electronics cards: an RTG4 [a low-power field-programmable gate array (FPGA)] based processor card that runs flight software, an output module card with seven switched bus power services and two unswitched services, a low-voltage power supply card that distributes secondary voltages to the ICDU cards, a housekeeping card that provides analog telemetry conditioning, two heater module cards each with 16 heater switches fed by bus power (32 total heaters), and a thermal control card with eight linearly regulated trim heater services.

K. Mechanism Control Electronics (MCE)

The primary purpose of the MCE is to drive the rotating telescope system. In addition, the MCE also drives the Solar Calibrator mechanism during the collection of calibration data in orbit. These operations are accomplished by motor controllers and position sensors. The MCE consists of three largely similar motor controller cards: two RTA/HAM controller cards (with independent A side and B side for redundancy), a solar calibrator controller card, a quiet regulated secondary power card, and a power filter card which prevents electrical noise from getting back into OCI or the PACE observatory.

Either side of the RTA/HAM controller cards can be powered by the ICDU and each receives the reference instrument clock from the DAU, which synchronizes the spinning of the RTA and HAM to the collection of science data in the FPAs.

III. OCI Radiometric Performance

The main output of OCI is a series of digital numbers (DNs), spatially and spectrally aggregated by the DAU (Section II-E). For each baseline mode science scan, there are 1272 spatial pixels per scan for the Earth view scan angle range, with each spatial pixel containing one DN for each spectral band, with a total of 291 bands. In addition, every scan collects 57 pixels when looking into the scan cavity at $+180^\circ$ scan angle, see Fig 1. These pixels are referred to as dark view pixels; they measure the dark offset for each band. It is assumed that this offset is constant during a scan, and the offset is subtracted from the Earth view DN via

$$\mathrm{d}n = \mathrm{DN} - \mathrm{DN}_0 \tag{1}$$

where DN_0 is the average per scan of the dark view pixels.

The OCI calibration equation converts Earth view dn to TOA radiance

$$L_t = K1 \cdot K2(t) \cdot [1 - K3 \cdot (T - T_{\mathrm{ref}})] \cdot K4(\theta) \cdot K5(\mathrm{d}n) \cdot K\mathrm{p} \cdot \mathrm{d}n \tag{2}$$

where

L_t	TOA radiance [W/(m^2 μm sr)];
$K1$	absolute gain factor [W/(m^2 $\cdot$ μm $\cdot$ sr)/dn];
$K2(t)$	relative gain factor as a function of time t, normalized to first on-orbit data acquisition; unitless;
$K3$	temperature correction [(°C)$^{-1}$];
T	temperature at relevant locations [°C];
T_{ref}	reference temperature [°C];
θ	scan angle [°];
$K4$	RVS; unitless;
$K5$	nonlinearity factor; unitless;
$K\mathrm{p}$	polarization correction; unitless;
dn	dark-corrected instrument counts [dn].

Results for $K1$–$K5$ and $K\mathrm{p}$ will be described in the following subsections, in addition to other performance parameters.

A. Spectral Characteristics

The OCI spectral characteristics were determined by sweeping a monochromatic source across the OCI spectral range. The test program used the Goddard Laser for Absolute Measurement of Radiance (GLAMR) as a tunable monochromatic source [39]. The laser source was fed into a 20-in integrating sphere with three National Institute of Standards and Technology (NIST) traceable calibrated radiometers. The integrating sphere was placed 8 in in front of a TVAC chamber window, with the center of the integrating sphere's 8-in aperture aligned to the OCI's nadir direction. For the calibration of the GLAMR radiances, the NIST traceable sources were placed into the TVAC chamber before OCI was put into the chamber, looking at the integrating sphere through the TVAC chamber window, thereby accounting for any light loss due to the window.

The laser source was swept in 1-nm steps from 310 to 2400 nm for in-band (i.e., high sensitivity of OCI) wavelengths. Four 10-nm wide regions (centered at 347, 555, 620, and 870 nm) were swept in 0.2-nm steps. Out-of-band (low sensitivity of OCI) regions in the SWIR (900–2400 nm) were swept in 10-nm steps. In-band radiance was set by GLAMR to 90% of L_{max} (maximum radiance expected on orbit) or L_{clip} (maximum radiance defined for high gain bands) or the maximum available GLAMR radiance (below 350 nm). Out-of-band radiance in the SWIR region was set to output the maximum available radiance by GLAMR. A detailed description of the measurements and analysis results has been provided by Kitchen-McKinley et al. [40].

The measurements acquired with GLAMR are the most important measurements of the OCI test campaign. A total of 11 requirements were verified with this dataset. Two of the key performance parameters of OCI are the center wavelengths (CWLs) and bandwidths of each OCI band. They are provided in numerical form for download at [41].

The absolute spectral response (ASR) can be calculated by dividing the dn OCI measured when looking at the integrating sphere's 8-in aperture by the radiance measured by the three NIST traceable radiometers. The relative spectral response (RSR) is the ASR divided by its maximum value. The RSR for all bands in baseline mode (interpolated to a 0.1-nm grid) is also provided at [41] for users in need of more spectral information than just CWLs and bandwidths.

The default 1-nm GLAMR sampling is not sufficient to accurately characterize the RSR of the hyperspectral bands, due to their narrow bandwidth of $\sim$5 nm. A 0.2-nm sampling is sufficient, but could not be acquired for the whole spectral range due to time constraints. The OCI team used three approaches to derive the optimal in-band (RSR $>$ 0.01) RSR. Common to all approaches is that a reference in-band RSR shape was derived, and the CWL and bandwidth were adjusted to the RSR measured of the individual band. The three approaches are as follows.

1) Derive the reference in-band RSR shape from the 0.2-nm measurements.
2) Same as 1), but adjusting the RSR shape by component level throughput measurements.

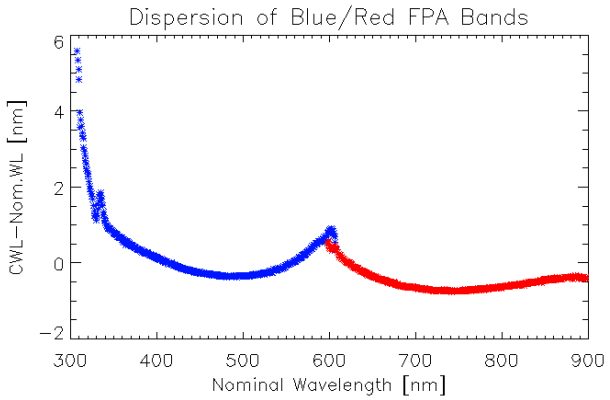

Fig. 6. OCI dispersion, expressed as the difference between measured CWL and nominal (design target) wavelength. The abscissa shows the nominal wavelengths with a spectral sampling of exactly 0.625 nm. The CWL was calculated as the FWHM of the RSR, see [40].

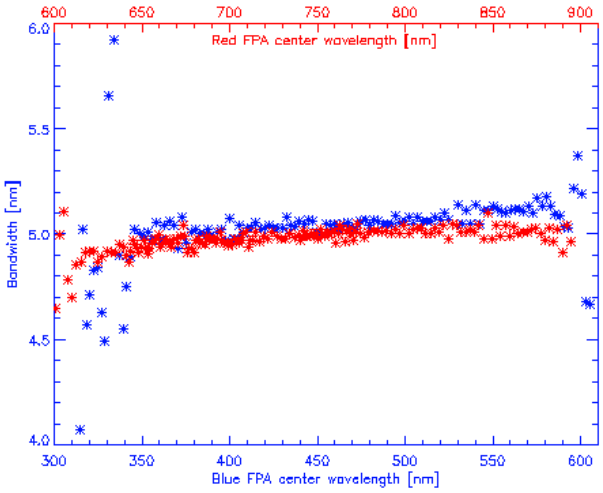

Fig. 7. OCI bandwidths for blue and red FPA bands in baseline mode.

3) Combine the 1-nm RSR measurements of all bands from a tap into a reference RSR shape for that tap. This provides improved wavelength sampling because the CWLs of the bands increase in steps of 0.625 nm, whereas the GLAMR wavelength step is 1.0 nm.

For each OCI band (480 per CCD), the approach was chosen that provided the smallest residuals to the RSR measurements of the respective band. Fig. 6 shows that above 340 nm, the deviation of the measured CWLs from the design target is: 1) a smooth function of wavelength and 2) within 1 nm of the design target. The data below 340 nm is less reliable due to low light levels of the laser source, but the strong deviation from the design target (up to 5.5 nm) is likely real.

For the baseline mode RSR, eight RSRs measured without spectral aggregation were aggregated into the RSR of a baseline band. The baseline mode spectral sampling is 2.5 or 1.25 nm, see Table II. The region around 670 nm was chosen for higher spectral sampling to support fluorescence line height [42] characterization in the ocean; the region around 760 nm was chosen to sample the oxygen A-band absorption in the atmosphere for aerosol layer height [43] and cloud top height [44]. Note that the bandwidth of each baseline mode band is independent of the spectral sampling, as shown in Fig. 7 (consistent bandwidth from 650 to 800 nm, for spectral sampling of either 1.25 or 2.5 nm, see Table II), because the L1B ground processing always aggregates to eight spectral pixels, see Section II-E. As expected, the spectral variation of the bandwidth seen in Fig. 7 is largest in the deep UV and the dichroic transition region around 600 nm (from 590 to 610 nm, both the red and blue FPA can receive significant amounts of light). Note that below 340 nm, measurement accuracy was compromised due to low GLAMR intensities.

In baseline mode, the L1B CWLs range from 314.6 to 605.5 nm on the blue FPA (119 bands total) and from 600.5 to 894.6 nm on the red FPA (163 bands total). For higher level processing (e.g., for L2 data, see [32] for data level definitions), the blue bands above 600 nm will be discarded. The original intent was to combine them with the red channel data up to 605 nm to increase SNR, but the radiometric accuracy of the red FPA data is superior (because of lower stray light, see below).

TABLE III
SWIR BAND SPECTRAL PARAMETERS

Band Name	CWL [nm]	FWHM [nm]	IOOB [%]	Lsat [W/m^2/µm/sr]
940	939.7	44.3	0.20	279.4
1038	1038.3	74.4	0.13	122.6
1250SG	1250.4	28.5	0.16	183.2
1250HG	1248.5	28.6	0.13	90.5
1378	1378.2	14.4	0.19	176.3
1615SG	1619.6	73.7	0.11	81.9
1615HG	1618.0	73.6	0.11	42.6
2130	2130.6	49.3	0.12	28.2
2260	2258.4	72.8	0.18	20.3

The integrated out-of-band response ratio (IOOB) describes the response of a band to light with wavelengths outside the extended bandpass. For OCI, IOOB is defined as the ratio of the integral of RSR over wavelength where RSR < 0.01 to the integral where RSR > 0.01, see [40]. For the blue FPA bands above 340 nm, IOOB is typically 2%–3.5%, and less than 1% for the red FPA bands, see [40]. The high blue channel IOOB is likely due to larger stray light caused by the blue grating, see also Section III-J. For wavelengths below 340 nm, IOOB increases significantly due to the low throughput at those wavelengths.

The spectral parameters of the SWIR bands are provided in Table III. Note that the CWLs of the high gain bands at 1250 and 1615 nm differ slightly from the corresponding standard gain bands (by 1.9 and 1.6 nm, respectively). The CWL of individual SDS units vary (by ± 1.4 and ± 1.2 nm for the two high gain bands, resp., see [45]). The CWL provided in Table III are averaged over SDS units (because of the TDI in baseline mode) and agree very well with the subsystem level measurements presented in [45].

The SWIR bandwidths are provided as the full-width half-maximum (FWHM) of the RSR measurements. The

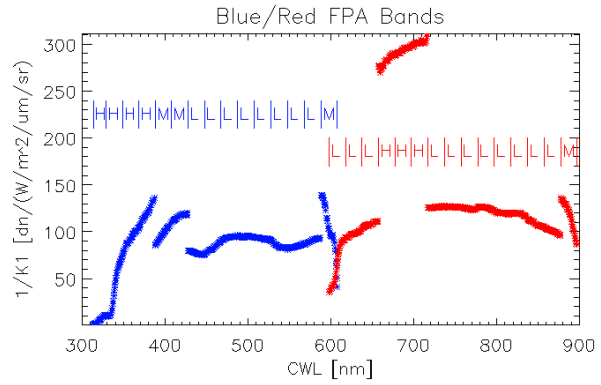

Fig. 8. OCI radiometric gains ($1/K1$) for blue and red FPA bands without spectral aggregation (32 bands per CCD tap). The tap gain settings are shown as H, M, and L for high, medium, and low.

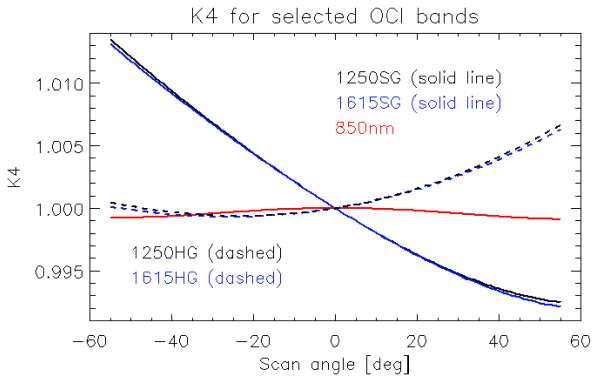

Fig. 9. $K4$ (RVS) for 850 nm and SWIR bands with identical MLA positions (see Table I). The 850 nm and 1250SG curves are 4th-order polynomial fits to system level measurements of the respective bands. $K4$ at 1615SG is calculated by adding the 1250SG curve and the difference of the $K4$ derived from component level (HAM only) reflectance measurements at 1615 and 1250 nm. Component level $K4$ for wavelengths above 850 nm (including all SWIR bands) are similar in magnitude to the system level $K4$ at 850 nm shown above, the MLA dependence (presumably vignetting) dominates the system level $K4$ of both 1250SG and 1615SG. Different MLA positions of the corresponding high gain bands (dashed lines) cause a very different $K4$ relative to the standard gain bands.

bandwidths were designed to maximize SNR while reducing the impact of nearby atmospheric absorption bands.

The IOOB shown in Table III is 0.2% or less. The low IOOB for the SWIR bands is due to their high-quality spectral bandpass filters. L_{sat} is discussed in Section III-G.

B. Gains (K1)

The radiometric gain (or $1/K1$) of each band can be calculated with (2), or by integrating the ASR over wavelength [46]. The former approach will be used on-orbit (see Section III-L), the results from the latter are shown in Fig. 8. The different gain settings of the OCI CCD taps can be seen clearly as sharp transitions. Steep gradients are caused by the dichroics (600 and 900 nm) and the decline in mirror reflectance below 350 nm.

C. Temperature Dependence (K3)

The radiometric sensitivity of OCI with regard to temperature variations ($K3$) was characterized during the OCI TVAC. The temperatures of several OCI subsystems (detectors, electronics, and optics) were individually cycled through the expected on-orbit temperature ranges. During the temperature cycles, OCI viewed a constant (after drift correction) light source through a window in the TVAC chamber. Equation (2) was used to derive $K3$ for all OCI bands. Typically, the radiance changed by less than 0.1% per degree temperature change for the temperature cycles of the detectors, much less when cycling the electronics or optics. The system level measured $K3$ for the detector cycle agreed very well with predictions based on component measurements.

A validation temperature cycle was performed where the whole OCI instrument was cycled through its on-orbit temperature range. The resulting uncertainties due to the temperature sensitivity of OCI after correction are typically about 0.1%. Note that below 340 nm, the light source was not bright enough to derive reliable $K3$ values. A detailed analysis of the OCI temperature sensitivity measurements has been published by Eplee [47].

The on-orbit temperature correction will use the detector temperatures of the respective bands (blue CCD temperature, red CCD temperature, and SWIR photodiode temperature), and the temperature of the lens housing for selected bands of the blue and red FPAs near the lower and upper limits of the spectral ranges for the two FPAs.

D. Response Versus Scan (K4)

The RVS or $K4$ was measured by placing OCI on a rotating platform, looking at a stationary 20-in integrating sphere with an exit aperture of 8 in, see [48]. OCI was rotated around its telescope spin axis to achieve different scan angles when looking at the exit aperture. The light output from the sphere was monitored for temporal drift using an internal hyperspectral radiometer. For the hyperspectral bands, the measured $K4$ agreed with model predictions based on component-level measurements of the HAM directional reflectance. The maximum $K4$ variation within the earth view scan angle range was 6.4% at 380 nm. However, for the SWIR bands below 1400 nm (InGaAs detectors), a significant dependence of $K4$ (up to 4%) on MLA position was seen that was not predicted [28]. The most likely explanation is vignetting in the MLA.

The SWIR bands above 1400 nm cannot be measured with the above setup, because the HgCdTe detectors need to be cooled (and the rotating platform did not fit into the TVAC chamber). We calculated $K4$ for the HgCdTe bands using component level HAM reflectance measurements and the $K4$ dependence on MLA position measured for the InGaAs bands (see Fig. 9), but this solution is not as reliable as for the other bands. Therefore, we assigned a higher uncertainty to $K4$ for the HgCdTe bands, see Section III-M, based on conservative estimates regarding potential differences in the light path as the wavelengths increase. We expect that validation with on-orbit data will show that our $K4$ uncertainty estimate for the highest wavelengths is very conservative.

As for $K3$ (see Section III-C), $K4$ for bands below 340 nm were not well characterized due to low light levels from

TABLE IV
SPATIAL PARAMETERS OF OCI SCIENCE PIXELS. SEE SECTION III-I

Band	**350nm**	**865nm**	**2260nm**
IFOV [deg] cross track	0.0893	0.0889	0.0878
IFOV [deg] along track	0.0917	0.0917	0.0911
GSD [deg] cross track	0.0888	0.0888	0.0888
GSD [deg] along track	0.0881	0.0881	0.0881
Field-of-Regard [deg]	112.9	112.9	111.7
MTF@Nyquist cross track	0.53	0.61	0.49
MTF@Nyquist along track	0.52	0.58	0.48

TABLE V
OCI SYSTEMATIC UNCERTAINTY ($k = 1$) ESTIMATE FOR SELECTED BANDS. SWIR BANDS ARE SHOWN FOR HIGH GAIN

Band [nm]	**350**	**443**	**555**	**865**	**1250**	**1615**
Total Systematic Uncertainty (RSS) [%]	1.27	0.73	0.74	0.72	1.42	1.80
K1 [%]	1.22	0.63	0.63	0.55	1.26	1.45
K2 [%]	0.12	0.12	0.11	0.11	0.11	0.12
K3 [%]	0.13	0.06	0.03	0.03	0.04	0.04
K4 [%]	0.02	0.01	0.01	0.01	0.01	0.72
K5 [%]	0.02	0.06	0.04	0.20	0.33	0.48
Kp [%]	0.06	0.05	0.05	0.06	0.06	0.04
Hysteresis [%]	N/A	N/A	N/A	N/A	0.41	0.45
Straylight/Crosstalk [%]	0.07	0.08	0.13	0.18	0.27	0.27
RSR [%]	0.27	0.33	0.34	0.32	0.10	0.10
SWIR fiber stability [%]	N/A	N/A	N/A	N/A	0.08	0.09
ADC power cycling [%]	0.07	0.07	0.07	0.07	N/A	N/A
Bit truncation [%]	0.01	0.02	0.02	0.11	N/A	N/A
CCD pulses and EMI noise [%]	0.1	0.1	0.1	0.1	0.1	0.1

the sphere. Nevertheless, the $K4$ accuracy is very small (see Table V) down to 340 nm, mainly due to the use of the EQ-400 from Energetiq [49], a laser-driven plasma lamp that provided high radiances above 340 nm with excellent temporal stability.

Another key to the excellent accuracy achieved for the RVS characterization was the capability of the rotating platform to quickly and accurately rotate OCI. Unfortunately, the RVS measurement at the solar diffuser angle required a repositioning of OCI on the platform, leading to a higher RVS uncertainty at the solar diffuser scan angle (up to 0.3% below 900 nm, up to 1.2% for the SWIR bands). Note that this impacts only the uncertainty of the on-orbit calculation of K1, not the RVS uncertainty of the Earth view data (see Table V).

E. Linearity (K5)

OCI linearity ($K5$) above 340 nm was characterized with two different approaches: measurements of white light in PTDI mode (progressive TDI, see [50]) and measurements of monochromatic light with regular TDI mode (using GLAMR as a source, providing calibrated radiances at different intensities). These two approaches are completely independent, the former essentially varies the OCI integration time for a constant source radiance, and the latter provides radiances at different intensities for a constant OCI integration time.

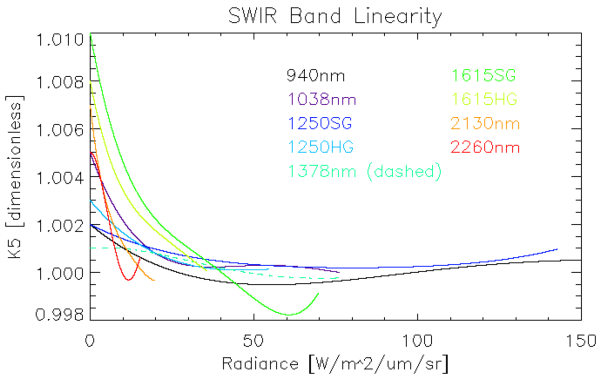

Fig. 10. $K5$ for the SWIR bands as a function of radiance.

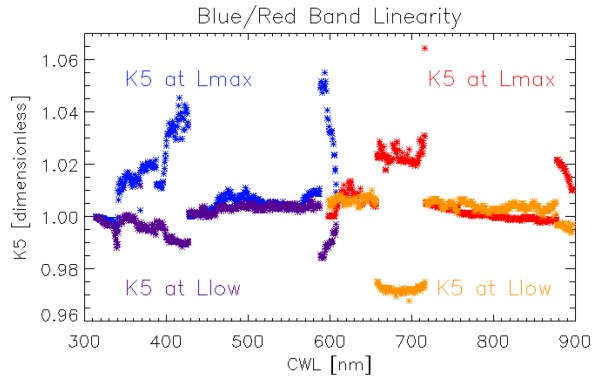

Fig. 11. $K5$ for the blue and red FPA bands at $L_{\max}$ and L_{low} as a function of CWL.

The two methods provided very similar results, see [28]. Due to time constraints, GLAMR was only used at selected wavelengths, and the $K5$ values shown here for bands above 340 nm and below 900 nm are from the PTDI measurements.

$K5$ for the SWIR bands was derived only with GLAMR. For wavelengths below 340 nm, $K5$ was derived with FPA level measurements, i.e., before integration of the blue FPA into OCI, illuminating the CCDs directly without the OCI optics.

No significant temperature dependence of linearity was found for any of the OCI bands (within the expected on-orbit temperature range).

The nonlinearity of the SWIR bands is generally low (below 1%, see Fig. 10), and lower for the InGaAs bands than for the HgCdTe bands.

For the hyperspectral bands, linearity is mainly introduced by the CCD sense node and FET output stage and is, therefore, strongly influenced by the tap gain setting (high gains causing larger nonlinearities). The variation over the dynamic range from the lowest ocean radiance (L_{low}) to the brightest cloud radiance ($L_{\max}$) can be several percent, see Fig. 11. It is obvious that a highly accurate linearity correction is needed. The uncertainty of the linearity correction is on the order of 0.1% for the hyperspectral bands at ocean-level radiances, but typically higher in the SWIR bands (up to 0.4%), see Table V.

For the SWIR bands, frequency-dependent nonlinearity was characterized as well [51]. The frequency dependency was about 0.1%. This value was added to the uncertainty of the nonlinearity correction for the SWIR bands.

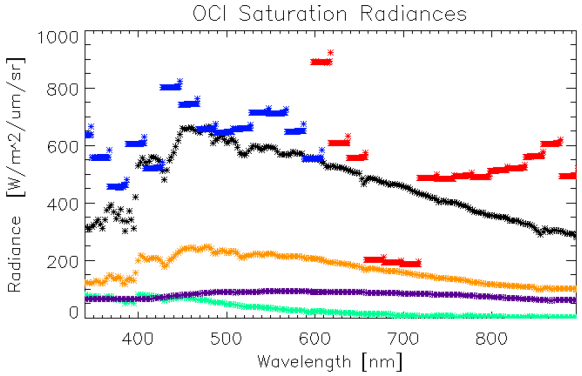

Fig. 12. OCI saturation radiances for the blue and red channels (no spectral aggregation) shown as blue and red symbols, respectively. L_{max}, L_{typ}, L_{bright}, and L_{lunar} are shown in black, green, orange, and purple, respectively.

F. Polarization (Kp)

The prelaunch characterization campaign showed that the OCI depolarizer works as intended, reducing the polarization sensitivity to less than 0.5% for all wavelengths above 350 nm [52], with an average value of about 0.2%. There is no significant variation with scan angle. There is a strong increase in polarization sensitivity below 350 nm. The intensity of the light source was too low to measure polarization below 330 nm. It might be possible to derive polarization sensitivities below 330 nm from on-orbit data, with a similar approach as used by Kwiatkowska et al. [53] for MODIS. Compared to heritage sensors such as MODIS and VIIRS, OCI has a very low sensitivity to polarization above 350 nm.

G. Saturation

The OCI requirements regarding saturation balance the opposing goals of high dynamic range (desire to measure radiances at the brightest cloud level (L_{max})] and high SNR at low radiance levels (for ocean color products, L_{typ}). The large difference between L_{max} and L_{typ} is shown in Fig. 12, demonstrating the challenges associated with achieving both goals simultaneously, especially above 700 nm. Most OCI bands are required to saturate above L_{max}, but certain bands were exempted because they are not critical for cloud products.

Fig. 12 shows the measured saturation levels for the blue and red channels, obtained by OCI in PTDI mode (see Section III-E) measuring white light from an integrating sphere. In the blue channel, small levels of saturation are observed around 420, 480, and 595 nm.

For the red channel, saturation occurs below L_{max} for the high gain bands from 658 to 717 nm, due to the high gain settings for the fluorescence line height bands (see Fig. 8). A partial aperture block had been installed between the red dichroic and the red grating to increase saturation radiances (by about 15%). As a result, no band saturates below the on-orbit calibration radiances (solar diffuser radiances (L_{bright}) and lunar radiance (L_{lunar}), see Fig. 12).

The SWIR bands saturate according to Table III, see also discussion in Section II-A. The light reaching the SWIR FPA is reduced by 15% with a partial aperture blocker to ensure the bands for cloud applications do not saturate.

H. SNR

The OCI SNR was measured in TVAC as a function of radiance. Typical radiances (L_{typ}) were defined for ocean [54] and cloud scenes, and the SNR requirement was evaluated at L_{typ}. L_{typ} is shown in Fig. 12, SNR in Fig. 13. OCI exceeds its SNR requirements with a significant margin for all bands (by at least 22%, typically around 80%). The UV-enhanced Ag coating on the mirror surfaces was critical in achieving a very good performance down to 345nm, the high gain taps for the fluorescence line height bands around 670 nm increased SNR as expected.

I. Spatial Characteristics

The spatial characteristics of the OCI data were measured with the "line spread function (LSF) bench." A collimated source was developed to simulate various scenes (e.g., a single illuminated Science Pixel surrounded by dark pixels) in order to evaluate the spatial performance of OCI. A 2-in integrating sphere was illuminated with either halogen sources or fiber-fed by GLAMR for monochromatic tests. Si and InGaAs detectors monitored the signal in the sphere. Attached to the sphere aperture are interchangeable scene masks which were precision-cut to simulate scenes (e.g., 1 × 1 km and 7 km (cross track) × 1 km (along track), slanted slit). The sphere illuminates an OAP that collimated the light before being projected into the OCI aperture, see [55] for further details.

The results for various spatial characteristics such as IFOV of a Science Pixel, ground sampling distance (GSD), MTF, and field of regard (FoR) are provided in Table IV for representative wavelengths. Variation among the hyperspectral bands was usually very small. For the SWIR bands, significant variations between bands were found, e.g., for IFOV cross track (standard deviation of 2%) and MTF cross track (standard deviation of 6%). These variations are likely due to the hysteresis effects discussed in Section III-K. The FoR for the SWIR bands differs slightly from the hyperspectral bands (from 0.1° to up to 1.2°) due to the position of the respective band on the MLA provided in Table I. By design, GSD depends mainly on the telescope rotation speed and detector readout rate and does not vary with wavelength.

Using a special time delay mode [56], the image acquisition start within the scan can be delayed in increments of 1/64th (1/32nd for the SWIR bands) of a Science Pixel for consecutive data collects, allowing a very fine sampling of a stationary setup like the LSF bench. Measurements with this mode are shown in Fig. 14. The IFOV in the scan direction can be derived from the FWHM of these curves.

The IFOV in track direction was derived from measurements of a slanted slit with a precisely known slant angle, results are reported in Table IV. A different method (tilting the OCI in the track direction relative to the LSF bench in 1/8th Science Pixel increments) produced about 5% lower IFOV in the track direction. This difference was not resolved, we are reporting the values from the former method because it was spectrally consistent, and the HgCdTe detectors could not be measured with the tilt approach.

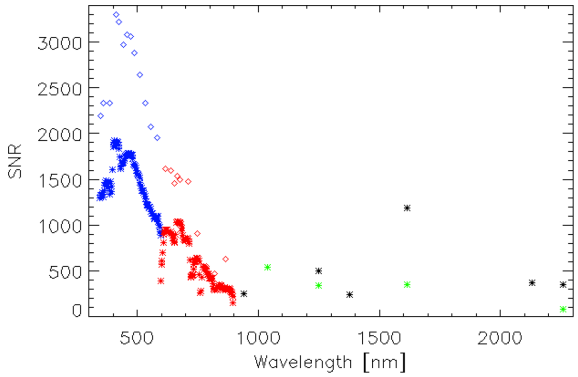

Fig. 13. OCI SNR as measured during the TVAC campaign. Blue/red stars are the SNR for the hyperspectral 5-nm bands of the blue/red channels at ocean L_{typ}, blue/red diamonds for multispectral bands at ocean L_{typ}, black stars for the SWIR bands at cloud L_{typ}, and green stars for the SWIR bands at ocean L_{typ}. The multispectral bands below 900 nm are provided as reference points to heritage sensors. They are typically 15-nm wide (40 nm for the 865-nm band), see [1] for their exact specifications.

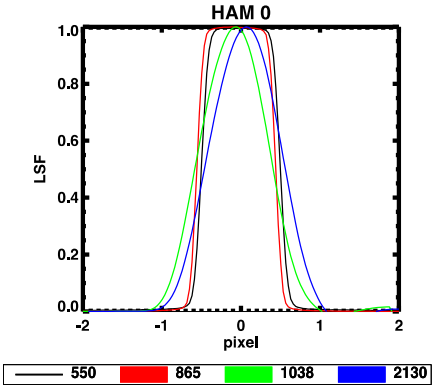

Fig. 14. IFOV measurements with time delay mode [56]. This figure shows the normalized OCI response to a one physical (CCD) pixel wide mask. OCI data at 550 and 865 nm has a spatial aggregation of 8.

Whereas the CCD bands are aggregated from eight 125-m pixels, the natural resolution of the SWIR bands is 1 km. These two different mechanisms can be clearly seen in Fig. 14: the combination of the eight 125-m pixels forms a plateau, whereas the SWIR bands show a rounded peak.

Band-to-band registration is defined as the minimum overlap of the area imaged by a certain band with any other band. The spectral variation of the imaged area in the track direction is small by design (±0.03 science pixels). However, there is variation in the cross track (scan) direction, see Fig. 15. Whereas the hyperspectral bands are tightly clustered (±0.005 science pixels), there is a significant variation for the SWIR bands (up to 0.3 science pixels), due to different delays caused by different electrical filter bandwidths.

J. Straylight and Crosstalk

Straylight and crosstalk are usually caused by optical scattering within the instrument, artifacts within the detector, or electronic features when processing the detector signal. For the purpose of this article, we define straylight as light at a certain wavelength, originating from a 1 × 1 km Science Pixel on the (Earth's) surface, entering the OCI telescope, that is recorded by OCI at the correct wavelength, but at a different

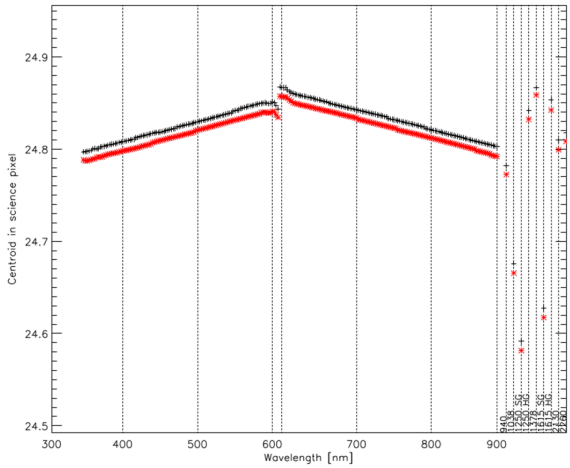

Fig. 15. Centroid in science pixels in cross track direction. Black and red are for the two HAM sides.

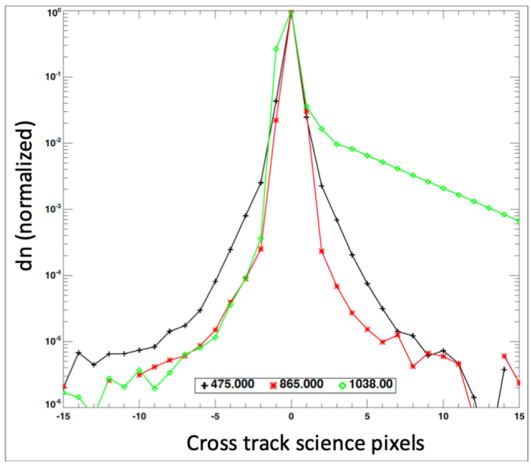

Fig. 16. OCI measured straylight as a function of cross track science pixels. The red band (red line: 865 nm) has the smallest straylight. The SWIR band (green line: 1038 nm) has the same order of magnitude of straylight before the peak as the red band, but a much higher response after the peak (hysteresis, see Section III-K). The blue band (black line: 475 nm) shows more straylight than the red band both before and after the peak.

spatial pixel. Light that is recorded by OCI at a different wavelength and at an incorrect spatial pixel is referred to as crosstalk. (Light that is recorded at the correct spatial pixel, but at the wrong wavelength, is IOOB, see Section III-A.)

The OCI straylight performance is shown in Fig. 16. Both the red and blue channels show very low straylight, especially the red channel. The higher straylight in the blue channel could be caused by scattering of the blue grating and/or the blue lens assembly.

The large response after the peak for the SWIR band will be discussed in the following section. The low response before the peak shows that optical scattering is low for the SWIR bands.

The blue channel has distinct optical crosstalk features, see Fig. 17, colloquially referred to as 'ghosts'. Based on their unique spectral signature (decreasing receiver wavelength for increasing sender wavelength, see [57, Fig. 6]), these ghosts have been identified as reflections of the CCD back to the grating, and then back to the CCD (see Fig. 2). The ghosts

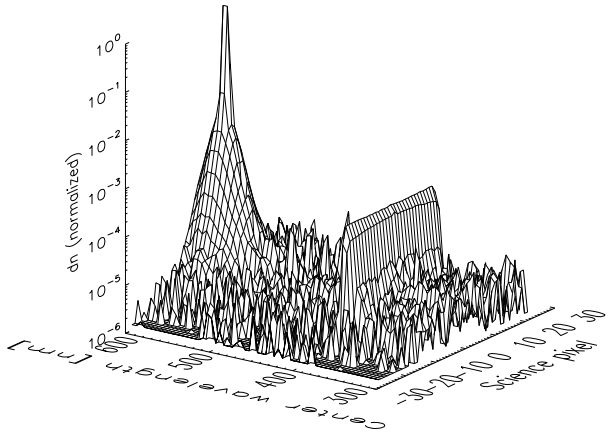

Fig. 17. OCI ghost [57] seen in the blue CCD response (normalized dn, spectral and spatial aggregation of 8), measured with a 1 science pixes mask in the LSF bench at Science Pixel 0, for a monochromatic source (sender) wavelength of 583 nm. The ghost for this sender wavelength appears at 383 nm. It is a 31 Science Pixel wide blade-like feature, due to the TDI data acquisition in the CCD. As the wavelength of the source wavelength decreases, the "blade" moves to higher wavelengths.

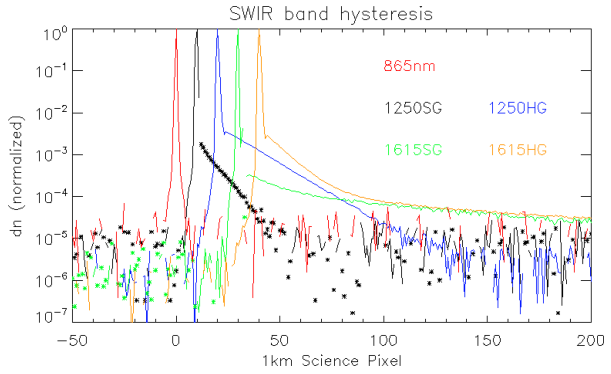

Fig. 18. OCI measurements of the 1SP mask in the LSF bench. SWIR band responses are successively offset by 10 pixels for plotting purposes. The negative values of the 1250SG (standard gain) and 1615SG bands are shown as stars in absolute values to emphasize the negative overshoot after the peak (only one pixel for 1615SG and about 30 pixels for 1250SG).

occur only in the blue CCD. A correction algorithm has been derived, its effectiveness will be evaluated on-orbit. The magnitude of the ghosts is small, but if the impact is noticeable in on-orbit images, the correction will be applied.

K. SWIR Band Hysteresis

During testing of the OCI ETU with the LSF bench, strong hysteresis after a radiance gradient was detected in the SWIR bands [27]. OCI flight unit measurements for selected bands are shown in Fig. 18. The 865-nm band is shown to demonstrate the desired response. All SWIR bands show significantly larger response after the peak, and negative dn values [i.e., DN values smaller than the dark current DN_0, see(1)] for some bands (up to 0.1% of the peak for the 1250SG band, see Fig. 18). The underlying cause was identified as slow traveling carriers from certain regions in the photodiodes [31], [58] (for both InGaAs and HgCdTe detectors) and suboptimal tuning in the electronic front end design of the detector readout circuit. Incorrect FEE tuning can result in negative dn after the response peak [31].

Unfortunately, schedule constraints did not allow an effective hardware remediation. Instead, an expanded test program was implemented for OCI flight unit testing that provided a comprehensive characterization of the effect. The LSF bench was used with masks of different widths (1, 2, 4, and 7 science pixels) and with different light intensities to confirm that the effect is linear/additive with regard to the radiance level and the spatial extent of the impulse. No temperature dependence of the effect was detected over the expected range of on-orbit temperatures.

Based on this test data, a correction algorithm was developed that reduces the impact to the noise level starting four science pixels after the response peak [31]. This addresses the strongest impact of the effect (dark ocean pixels measured after cloud pixels), allowing the usage of SWIR bands for the common case in global TOA radiance images of large ocean areas next to extended cloud fields. Unfortunately, in the case of high-frequency radiance gradients in the along scan direction, the current version of the correction provides only limited improvement.

Several methods exist to monitor (and potentially improve) the current version of the correction once on-orbit. The SPCA (see Section II-I) will provide a daily measurement of the hysteresis effect for a very short impulse. A dedicated monthly lunar measurement (repeatedly scanning a line across the center of the moon, i.e., without along track progression, allowing to average of several scan lines to enhance the response far away from the moon) will provide a measurement with a more extended source (about 8-pixels wide). We also expect to be able to use a measurement where OCI scans across the Earth's limb toward deep space, providing a much wider impulse than we could test during the prelaunch campaign.

L. On-Orbit Performance Monitoring

On-orbit variations over time in the radiometric sensitivity of each OCI band are captured by the parameter $K2$. They will be monitored by: 1) solar diffuser measurements (daily and monthly, over the northern terminator) for short to medium-term instrument gain adjustments and 2) lunar irradiance measurements for trend adjustments over long time periods, similar to the approach used for the VIIRS instrument [59]. OCI is planning to measure the lunar irradiance twice per lunar month at $\sim 7^\circ$ phase angle. Dedicated lunar measurements will be performed in conjunction with these lunar irradiance measurements to measure hysteresis characteristics in the SWIR bands, supporting the SPCA measurements. Both the solar diffuser and lunar measurements require dedicated spacecraft maneuvers [60], [61].

Although the radiometric gains ($K1$) were measured prelaunch, we are currently planning to use the $K1$ derived from on-orbit measurements of the bright solar diffusers for processing science data products. This approach eliminates uncertainty due to any potential radiometric gain change from the time of OCI TVAC to the first on-orbit solar diffuser measurement. Reasonable agreement between the two methods would validate both.

On-orbit changes of the spectral characteristics of OCI will be monitored via measurements taken without spectral

aggregation (i.e., sampling at 0.625-nm intervals) from the solar diffuser measurements and from Earth view measurements (see Table II), using the known absorption characteristics of Fraunhofer lines and atmospheric absorption features (e.g., O_2A band) [62]. Unaggregated Earth view data will be acquired during selected tilt maneuvers, with a limited scan angle range ($\pm 16^\circ$ around the nadir) because the high data rate of the unaggregated mode requires a reduction in data volume. The geolocation of the Earth view data during the tilt maneuver will be less accurate, but accurate geolocation is not needed for this spectral analysis.

The dim diffuser will be measured monthly. The dim diffuser measurements will be acquired in progressive TDI (PTDI) mode (see Section III-E) to support trending of on-orbit linearity changes. Unfortunately, the BRDF of the dim diffuser ($\sim$0.023/sr) is higher than expected, limiting the dynamic range over which the linearity characterization can be performed: for bands above 580 nm, the radiance provided by the dim diffuser is higher than the typical ocean radiance (L_{typ}).

M. Uncertainty Estimate

Table V shows the systematic uncertainty estimate for OCI TOA radiances for selected wavelengths at typical ocean radiance levels. The table provides individual uncertainty components and the total uncertainty, calculated as the root mean square sum of the individual components. The uncertainty for $K1$ is calculated from the uncertainty of the bright solar diffuser measurements, including the RVS uncertainty at the solar diffuser scan angle. The $K1$ uncertainty is the dominant term for all bands.

Vicarious calibration [26] will be applied in the ocean color processing for wavelengths below 720 nm. (Note that it will not be applied for the processing of aerosol or cloud products.) The uncertainty of a vicariously calibrated band is independent of the solar diffuser calibration of that band, therefore $K1$ uncertainty becomes the uncertainty of the vicarious calibration process ($\sim$0.1%, see [26]). Note that vicarious calibration requires a large number of matchups of the in situ truth source to the satellite measurement in order to result in an uncertainty of 0.1%, so it will take at least a year of on-orbit data to achieve this accuracy. Recalculating for the case of vicarious calibration leads to a total uncertainty of $\sim$0.4% for most bands below 720 nm, meeting the goal for ocean color of 0.5% described by Gordon [24].

NASA has invested in improvements to the in situ sources for ocean color vicarious calibration. These developments are on schedule to provide data from the start of the PACE mission [63], [64]. In additon, matchups from the well-established MOBY buoy [65] will be available for vicarious calibration. For the first time, there will be sources of vicarious calibration data in each hemisphere.

The uncertainty estimates for OCI are a work in progress and will be updated after launch. We have confidence in most terms provided in Table V, but some items (e.g., the accuracy of the corrections for crosstalk and SWIR band hysteresis) will likely need revisions.

The top-level uncertainty requirements for the PACE science products are provided in Table I in [1]. The OCI systematic uncertainties combined with the SNR (see Section II-H) allow the production of the PACE ocean color products with a significant margin regarding their uncertainty requirements [66]. For the aerosol and cloud products, PACE requires a systematic uncertainty better than 5%, which is met by all bands with a margin of at least 2%.

IV. Conclusion

OCI is a complex instrument. A wide range of technology developments and design optimizations needed to be implemented to achieve the challenging PACE mission requirements, especially with regard to the uncertainty requirements for ocean color products. A comprehensive prelaunch characterization campaign was essential to achieving this high level of accuracy. The campaign verified that all the OCI science requirements [67] were met. The OCI test team built on the experiences of heritage test campaigns, incorporating state-of-the-art light sources such as NIST traceable tuneable lasers and plasma lamps. A wide variety of OCI image acquisition modes was essential for accurately measuring different characteristics of OCI.

Since the primary purpose of OCI is ocean color, some of the design choices made are not ideal for other science disciplines:

1) The OCI along track tilt is critical to avoid glint over ocean, but increases the path length through the atmosphere and results in suboptimal coverage in equatorial regions.
2) High spatial resolution was a lower priority than SNR, the capability to accurately characterize the radiometric output, and the avoidance of striping in the images.
3) At a few wavelength ranges, OCI saturates below cloud radiance levels in order to increase SNR at lower radiance levels.

Despite these compromises, OCI will be an innovative data source for many science applications, not just ocean color and atmospheric science. OCI will provide daily global coverage of TOA hyperspectral radiances below 900 nm, and multispectral radiances up to 2260 nm. Below 900 nm, the spectral sampling is 2.5 nm (1.25 nm in selected spectral regions), with a bandwidth of 5 nm. OCI will be the first sensor to provide hyperspectral daily global coverage, down to 340 nm. It will provide a total of 291 spectral bands in baseline mode, including bands down to 315 nm. However, the radiometric uncertainty of radiances from 315 to 340 nm is high and not discussed here. OCI has very low polarization sensitivity, and its radiances can be combined with the simultaneously acquired polarization measurements from the two multiangle polarimeters onboard the PACE spacecraft.

After the launch of the PACE mission in February 2024, OCI was successfully powered on and started its commissioning phase. The mission is designed to last at least 3 years; spacecraft fuel is sufficient for 10 years. OCI science data will be provided as open access by NASA's Ocean Biology Distributed Active Archive Center [68].

ACKNOWLEDGMENT

The authors would thank the whole OCI Team for their dedication to designing, building, and testing this instrument, including C. Albert, C. Auletti, S. Babu, B. Blagojevic, K. Boggs, G. Bredthauer, G. Brown, K. Burgundy, J. Butler, N. Cao, T. Capon, J. Carpenter, J. Champagne, F. Chi, C. Choi, B. Clemons, J. Cook, W. Cook, N. Costen, P. Coulter, K. Dahya, A. DiFatta, P. Dizon, R. Esplin, A. Feizi, S. Feng, R. Gheen, S. Gno, H. Gonce, J. Guzek, O. Haddad, C. Hakun, L. Haynes, S. Hawks, J. Hayden, M. Hersh, C. Hill, G. Hilton, M. Hinkle, D. Holiday, K. Jepsen, T. Johnson, E. Kan, B. Kercheval, S. Kholdebarin, J. Kline, R. Kinder, A. Korb, A. La, E. Laurila, M. Lin, J. Lobell, W. Lu, T. Madison, A. Mariano, L. Meier, B. Monosmith, P. Morey, B. Mott, M. Mulloney, K. Novo-Gradic, T. Nolan, Q. Nquyen, W. Ousley, M. Owens, J. Parker, D. Patel, J. Peterson, A. Poulin, M. Quijada, L. Ramos-Izquierdo, A. Repp, K. Ray, E. Rodriguez, A. Rosanova, K. Seaton, D. Senai-Alemou, S. Sharmin, D. Smallwood, D. Sohl, M. Sohl Smith, C. Stull, J. Thomes, Y. Wen, M. Wilson, G. Won, C. Zinke, and many others.

For their support for OCI calibration and data analysis, they would also thank J. Barsi, N. Collins, C. Field, J. Hedelius, B. McAndrew, J. McCarthy, K. Squire, R. Snel, A. Sushkov, B. Tse, E. Waluschka, and J. Zeng.

REFERENCES

[1] P. J. Werdell et al., "The plankton, aerosol, cloud, ocean ecosystem mission: Status, science," *Adv. Bull. Am. Meteorol. Soc.*, pp. 1775–1794, 2019.

[2] H. R. Gordon, *Physical Principles of Ocean Color Remote Sensing*. Coral Gables, FL, USA: University of Miami, 2019.

[3] H. M. Dierssen et al., "Living up to the hype of hyperspectral aquatic remote sensing: Science, resources and outlook," *Frontiers Environ. Sci.*, vol. 9, Jun. 2021, Art. no. 649528.

[4] I. Cetini et al., "Phytoplankton composition from space: Requirements, opportunities, and challenges," *Remote Sens. Environ.*, vol. 302, May 2024, Art. no. 113964.

[5] J. Chowdhary et al., "Modeling atmosphere-ocean radiative transfer: A PACE mission perspective," *Frontiers Earth Sci.*, vol. 7, p. 100, Jun. 2019.

[6] O. M. Coddington, T. Vukicevic, K. S. Schmidt, and S. Platnick, "Characterizing the information content of cloud thermodynamic phase retrievals from the notional PACE OCI shortwave reflectance measurements," *J. Geophys. Res. Atmos.*, vol. 122, no. 15, pp. 8079–8100, Aug. 2017.

[7] A. M. Sayer et al., "The CHROMA cloud-top pressure retrieval algorithm for the plankton, aerosol, cloud, ocean ecosystem (PACE) satellite mission," *Atmos. Meas. Techn.*, vol. 16, no. 4, pp. 969–996, Feb. 2023.

[8] C. R. McClain, G. C. Feldman, and S. B. Hooker, "An overview of the SeaWiFS project and strategies for producing a climate research quality global ocean bio-optical time series," *Deep Sea Res. Part II, Top. Stud. Oceanogr.*, vol. 51, nos. 1–3, pp. 5–42, Jan. 2004.

[9] W. L. Barnes, T. S. Pagano, and V. V. Salomonson, "Prelaunch characteristics of the moderate resolution imaging spectroradiometer (MODIS) on EOS-AM1," *IEEE Trans. Geosci. Remote Sens.*, vol. 36, no. 4, pp. 1088–1100, Jul. 1998.

[10] M. Rast, J. L. Bezy, and S. Bruzzi, "The ESA medium resolution imaging spectrometer MERIS a review of the instrument and its mission," *Int. J. Remote Sens.*, vol. 20, no. 9, pp. 1681–1702, Jan. 1999.

[11] J. Nieke, "The ocean and land colour imager (OLCI) for the Sentinel 3 GMES mission: Status and first test results," in *Earth Observing Missions Sensors: Development Implementing*, vol. 8528. Bellingham, WA, USA: SPIE, 2012, pp. 49–57.

[12] R. E. Murphy, P. Ardanuy, F. J. Deluccia, J. E. Clement, and C. F. Schueler, "The visible infrared imaging radiometer suite," in *Earth Science Satellite Remote Sensing*. Cham, Switzerland: Springer, 2006, pp. 199–223.

[13] J. V. Martins, R. Fernandez-Borda, B. McBride, L. Remer, and H. M. J. Barbosa, "The harp hype ran gular imaging polarimeter and the need for small satellite payloads with high science payoff for Earth science remote sensing," in *Proc. IEEE Int. Geosci. Remote Sens. Symp.*, Jul. 2018, pp. 6304–6307.

[14] O. P. Hasekamp et al., "Aerosol measurements by SPEXone on the NASA PACE mission: Expected retrieval capabilities," *J. Quant. Spectrosc. Radiat. Transf.*, vol. 227, pp. 170–184, Apr. 2019.

[15] M. Gao et al., "Simultaneous retrieval of aerosol and ocean properties from PACE HARP2 with uncertainty assessment using cascading neural network radiative transfer models," *Atmos. Meas. Techn.*, vol. 16, no. 23, pp. 5863–5881, Dec. 2023, doi: 10.5194/amt-16-5863-2023.

[16] N. K. Hannadige et al., "Atmospheric correction over the ocean for hyperspectral radiometers using multi-angle polarimetric retrievals," *Opt. Exp.*, vol. 29, no. 3, p. 4504, Feb. 2021, doi: 10.1364/oe.408467.

[17] W. W. Gregg and F. S. Patt, "Assessment of tilt capability for spaceborne global ocean color sensors," *IEEE Trans. Geosci. Remote Sens.*, vol. 32, no. 4, pp. 866–877, Jul. 1994, doi: 10.1109/36.298014.

[18] C. R. McClain et al., *Science and Observation Recommendations for Future NASA Carbon Cycle Research*, document NASA/TM-2002-210009, 2002.

[19] C. McClain, *The Ocean Radiometer for Carbon Assessment (ORCA): Development History Within an Advanced Ocean Mission Concept*, document NASA/TM-2012-215894, 2012.

[20] M. E. Wilson et al., "Optical design of the ocean radiometer for carbon assessment," in *Proc. SPIE*, Sep. 2011, p. 81530, doi: 10.1117/12.897023.

[21] B. Monosmith and C. McClain, *Ocean Radiometer for Carbon Assessment (ORCA) System Design and Radiometric Performance Analysis*, document NASA/TM-2012-215896, 2012.

[22] M. Gerhard, *Requirements for an Advanced Ocean Radiometer*, document NASA/TM-2011-215883, 2011.

[23] C. D. Castillo et al., *Pre-Aerosol, Clouds, and Ocean Ecosystem (PACE) Mission Science Definition Team Report*, document NASA/TM-2018-219027, 2018.

[24] H. R. Gordon, "In-orbit calibration strategy for ocean color sensors," *Remote Sens. Environ.*, vol. 63, no. 3, pp. 265–278, Mar. 1998.

[25] M. Wang and H. R. Gordon, "Calibration of ocean color scanners: How much error is acceptable in the near infrared?" *Remote Sens. Environ.*, vol. 82, nos. 2–3, pp. 497–504, Oct. 2002.

[26] B. A. Franz, S. W. Bailey, P. J. Werdell, and C. R. McClain, "Sensor-independent approach to the vicarious calibration of satellite ocean color radiometry," *Appl. Opt.*, vol. 46, no. 22, p. 5068, Aug. 2007.

[27] G. Meister et al., "Test results from the prelaunch characterization campaign of the engineering test unit of the ocean color instrument of NASA's plankton, aerosol, cloud and ocean ecosystem (PACE) mission," *Frontiers Remote Sens.*, vol. 3, pp. 1–15, Jun. 2022.

[28] M. Gerhard, "Initial look at the results from the prelaunch characterization campaign of OCI on the PACE mission," in *Proc. IEEE Int. Geosci. Remote Sens. Symp.*, May 2023, pp. 1345–1348.

[29] M. A. Quijada, M. Wilson, E. Waluschka, and C. R. McClain, "Optical component performance for the ocean radiometer for carbon assessment (ORCA)," in *Proc. SPIE*, Sep. 2011, p. 81530.

[30] U. Gliese et al., "Optical and detector design of the ocean color instrument for the NASA pace mission," in *Proc. IEEE Int. Geosci. Remote Sens. Symp.*, Jul. 2023, pp. 1337–1340.

[31] U. Gliese et al., "Pulse response of the shortwave infrared detection system of the ocean color instrument for the NASA PACE mission," in *Proc. Sensors, Syst. Next-Gener. Satell.*, Oct. 2023, p. 127290.

[32] (2021). *Earthdata*. [Online]. Available: https://www.earthdata.nasa.gov/engage/open-data-services-and-software/data-information-policy/data-levels

[33] J. Schepis, "The design & development of the ocean color instrument precision superduplex hybrid bearing cartridge," in *Proc. Aerosp. Mech. Symp.*, 2018, pp. 97–112.

[34] K. Yang, D. Patel, and W. Ousley, "NASA's PACE ocean color instrument thermal design evolution: From goddard's instrument design lab through flight development," in *Proc. 52nd Int. Conf. Environ. Syst.*, Jul. 2023, pp. 1–16.

[35] E. T. Gorman, D. A. Kubalak, D. Patel, D. B. Mott, G. Meister, and P. J. Werdell, "The NASA plankton, aerosol, cloud, ocean ecosystem (PACE) mission: An emerging era of global, hyperspectral Earth system remote sensing," in *Sensors, Systems and Next-Generation Satellites XXIII*, vol. 11151. Bellingham, WA, USA: SPIE, 2019, pp. 78–84.

[36] D. Steven and L. Bourg, "Radiometric calibration of MERIS," in *Sensors, Systems and Next-Generation Satellites*, vol. 7474. Bellingham, WA, USA: SPIE, 2009, pp. 258–269.

[37] (2024). *Fractal Black Coating*. Accessed: Mar. 5, 2024. [Online]. Available: https://acktar.com/product/fractal-black/

[38] C. Green, N. Haghani, A. Hernandez-Pellerano, B. Gheen, A. Lanham, and J. Fraction, "MUSTANG: A workhorse for NASA spaceflight avionics," *2023 IEEE 9th Int. Conf. Space Mission Challenges Inf. Technol. (SMC-IT)*, Pasadena, CA, USA, 2023, pp. 94–103, doi: 10.1109/SMC-IT56444.2023.00019.

[39] J. A. Barsi et al., "Spectral and radiometric performance of the Goddard laser for absolute measurement of radiance," in *Proc. Earth Observing Syst.*, Oct. 2023, p. 12685, doi: 10.1117/12.2678195.

[40] S. Kitchen-McKinley et al., "Pace OCI flight unit pre-launch spectral characterization," in *Proc. IEEE Int. Geosci. Remote Sens. Symp.*, Jul. 2023, pp. 1349–1352, doi: 10.1109/igarss52108.2023.10283202.

[41] *OB.DAAC*. Accessed: Mar. 5, 2024. [Online]. Available: https://oceancolor.gsfc.nasa.gov/data/pace/characterization/

[42] M. J. Behrenfeld et al., "Satellite-detected fluorescence reveals global physiology of ocean phytoplankton," *Biogeosciences*, vol. 6, no. 5, pp. 779–794, May 2009.

[43] S. Corradini and M. Cervino, "Aerosol extinction coefficient profile retrieval in the oxygen A-band considering multiple scattering atmosphere. Test case: SCIAMACHY nadir simulated measurements," *J. Quant. Spectrosc. Radiat. Transf.*, vol. 97, no. 3, pp. 354–380, Feb. 2006, doi: 10.1016/j.jqsrt.2005.05.061.

[44] M. Desmons, N. Ferlay, F. Parol, L. Mcharek, and C. Vanbauce, "Improved information about the vertical location and extent of monolayer clouds from POLDER3 measurements in the oxygen A-band," *Atmos. Meas. Techn.*, vol. 6, no. 8, pp. 2221–2238, Aug. 2013.

[45] J. K. Hedelius et al., "Infrared spectral responses of the ocean color instrument (OCI) pre-assembly and integration," *Earth Observing Syst.*, vol. 12232, pp. 283–290, Jun. 2022.

[46] R. A. Barnes, S. W. Brown, K. R. Lykke, B. Guenther, X. Xiong, and J. J. Butler, "Comparison of two methodologies for calibrating satellite instruments in the visible and near infrared," in *Proc. SPIE*, Oct. 2010, p. 78620, doi: 10.1117/12.868356.

[47] J. Eplee, "Prelaunch radiometric calibration of the thermal response of the PACE ocean color instrument," in *Earth Observing System*, vol. 12685. Bellingham, WA, USA: SPIE, 2023.

[48] J. J. Knuble et al., "Pre-launch calibration methods of OCI on the PACE mission," in *Proc. IEEE Int. Geosci. Remote Sens. Symp.*, Jun. 2023, pp. 1341–1344.

[49] (2024). *Energetiq,*. [Online]. Available: https://www.energetiq.com/ldls-eq400-laser-driven-light-source-broadband

[50] J. McIntire, S. Kitchen-McKinley, H. Choi, and G. Meister, "Progressive TDI measurements with the PACE OCI ETU," in *Proc. Earth Observing System*. Bellingham, WA, USA: SPIE, Aug. 2021, doi: 10.1117/12.2594239.

[51] K. J. Squire et al., "PACE OCI short-wave infrared detection assembly frequency-dependent linearity characterization and uncertainty analysis," in *Earth Observing System*, vol. 12232. Bellingham, WA, USA: SPIE, 2022, pp. 304–313.

[52] J. McIntire, E. Waluschka, G. Meister, J. Knuble, and W. B. Cook, "PACE OCI polarization sensitivity based on pre-launch testing," in *Earth Observing Systems*. Bellingham, WA, USA: SPIE, 2023. [Online]. Available: https://doi.org/10.1117/12.2677522

[53] E. J. Kwiatkowska, B. A. Franz, G. Meister, C. R. McClain, and X. Xiong, "Cross calibration of ocean-color bands from moderate resolution imaging spectroradiometer on terra platform," *Appl. Opt.*, vol. 47, no. 36, p. 6796, Dec. 2008.

[54] Z. Ahmad and G. Meister, *LTYP and Lmax Calculations for PACE Ocean Color Instrument, in PACE Technical Report Series*, document NASA/TM-2018-219027/, 2018.

[55] J. J. Knuble et al., "Measurement techniques for the high-contrast and in-field stray light performance of OCI," in *Sensors, System Next-Generation Satellites*, vol. 12729. Bellingham, WA, USA: SPIE, 2023, pp. 170–178.

[56] H. Choi, J. McIntire, S. Kitchen-McKinley, G. Meister, L. Chemerys, and S. Lee, "Spatial characterization of PACE OCI ETU using time-delay mode," in *Earth Observing Systems* (2022). Bellingham, WA, USA: SPIE, 2022, doi: 10.1117/12.2632640.

[57] L. Shihyan, G. Meister, S. Kitchen-McKinley, J. Knuble, U. Gliese, and R. Bousquet, "PACE OCI crosstalk characterization based on pre-launch testing," in *Sensors, Systems and Next-Generation Satellites XXVII*, vol. 12729. Bellingham, WA, USA: SPIE, 2023, pp. 341–349.

[58] G. George and J. P. Krusius, "Dynamic response of high-speed PIN and Schottky-barrier photodiode layers to nonuniform optical illumination," *J. Lightw. Technol.*, vol. 12, no. 8, pp. 1387–1393, Jul. 1994.

[59] R. E. Eplee, K. R. Turpie, G. Meister, F. S. Patt, B. A. Franz, and S. W. Bailey, "On-orbit calibration of the suomi national polar-orbiting partnership visible infrared imaging radiometer suite for ocean color applications," *Appl. Opt.*, vol. 54, no. 8, p. 1984, Mar. 2015.

[60] G. Meister and R. E. Eplee, *Strategy and Requirements for the PACE OCI Solar Calibration*, document NASA/TM-2018-219027, 2018.

[61] F. S. Patt and R. E. Eplee, *Strategy and Requirements for the PACE OCI Lunar Calibration*, document NASA/TM-2018-219027, 2018.

[62] S. Delwart, R. Preusker, L. Bourg, R. Santer, D. Ramon, and J. Fischer, "MERIS in-flight spectral calibration," *Int. J. Remote Sens.*, vol. 28, nos. 3–4, pp. 479–496, Feb. 2007, doi: 10.1080/01431160600821119.

[63] C. Susanne et al., "A hyperspectral, langrangian, profiling float for system vicarious calibration of PACE," in *PACE Technical Report Series, System Vicarious Calibration Technical Memorandum*. Greenbelt, MD, USA: National Aeronautics and Space Administration, Goddard Space Flight Center, 2024.

[64] C. Susanne et al., "MarONet—A new, moored platform for system vicarious calibration of PACE," in *PACE Technical Report Series, System Vicarious Calibration Technical Memorandum*. Greenbelt, MD, USA: National Aeronautics and Space Administration, Goddard Space Flight Center, 2024.

[65] S. W. Brown et al., "The marine optical buoy (MOBY) radiometric calibration and uncertainty budget for ocean color satellite sensor vicarious calibration," in *Proc. SPIE*, Oct. 2007, doi: 10.1117/12.737400.

[66] A. Ibrahim et al., *PyTOAST: A Python-Based Simulator for Hyperspectral Ocean Color Observations and Uncertainty Assessment*. Washington, DC, USA: American Geophysical Union, 2023.

[67] (2024). *OCI Requirements*. [Online]. Available: https://pace/oceansciences.org/requirements.htm

[68] (2024). *OB.DAAC*. [Online]. Available: https://www.earthdata.nasa.gov/eosdis/daacs/obdaac

Gerhard Meister received the Diploma and Ph.D. degrees in physics from the University of Hamburg, Hamburg, Germany, in 1996 and 2000, respectively.

From 2000 to 2010, he was with Futuretech Corporation, Goddard Space Flight Center (GSFC), Greenbelt, MD, USA, where he became a NASA Civil Servant at the Ocean Ecology Laboratory, in 2010. Since 2015, he has been the Instrument Scientist for the Ocean Color Instrument for NASA's Plankton, Aerosol, Cloud, ocean Ecosystem (PACE) Mission, GSFC. His main focus is on the calibration and characterization of satellite-based ocean color sensors.

Joseph J. Knuble received the B.S. degree in electrical and computer engineering from Worcester Polytechnic Institute, Worcester, MA, USA, in 2002, and the M.S. degree in electrical and computer engineering from Johns Hopkins University, Baltimore, MD, USA, in 2007.

In 2002, he joined the Microwave Instrument Technology Branch (Code 555), NASA's Goddard Space Flight Center, Greenbelt, MD, USA, where he designed active and passive microwave remote sensing instruments for 15 years. He was the Lead Engineer for the SMAP Radiometer Front-End which launched in 2015. In 2016, he joined the Ocean Color Instrument (OCI) Instrument Systems Engineering Team with a focus on calibration activities. In 2022, he became the Lead Instrument Systems Engineer for OCI, which launched aboard the Plankton, Aerosol, Cloud, ocean Ecosystem (PACE) mission in 2024. In 2023, he became the Principle Engineer for the Planetary Science Projects Division (Code 430) at GSFC.

Ulrik Gliese received the M.Sc.E.E and Ph.D. degrees from the Technical University of Denmark, Lyngby, Denmark, in 1989 and 1992, respectively.

Since 1992, he has led and performed research and development, covering a wide range of topics in the areas of microwave photonics, fiber-optic communication systems, wireless cellular communication networks, and space flight instruments including particle spectrometers, and optical imaging systems and spectrometers at the Technical University of Denmark, Corning, Corning, NY, USA, Corvis, Columbia, MD, USA, Infinera, Sunnyvale, CA, USA, Naval Research Laboratory, Washington, DC, USA, and NASA Goddard Space Flight Center (GSFC), Greenbelt, MD, USA. He was the Chief Engineer leading the development of the 16 dual-electron spectrometers on the NASA MMS 4-satellite constellation mission. Since 2015, he has been the Deputy Instrument Manager and Chief Engineer for the Ocean Color Instrument on the NASA Plankton, Aerosol, Cloud, ocean Ecosystem (PACE) Mission.

Robert Bousquet, photograph and biography not available at the time of publication.

Leland H. Chemerys, photograph and biography not available at the time of publication.

Hyeungu Choi received the bachelor's degree in imaging science and the master's degree in remote sensing from the Rochester Institute of Technology, Rochester, New York, in 1998 and 2002, respectively.

From 2002 to 2018, he served as a Supporting Scientist/Programmer at the NASA's Goddard Space Flight Center, Greenbelt, MD, USA, for Antarctica ice sheet analysis and Amazon fire/logging detection using various satellite images. He joined the Plankton, Aerosol, Cloud, ocean Ecosystem (PACE)/Ocean Color Instrument (OCI) Team in 2019 to support the characterization of OCI's spatial characteristics and calibration.

Robert E. Eplee received the B.S. degree in physics from the University of North Carolina, Chapel Hill, North Carolina, in 1981, and the Ph.D. degree in planetary sciences from the University of Arizona, Tucson, AZ, USA, in 1987.

He has been serving as an Instrument Calibration Scientist for the NASA Ocean Biology Processing Group, NASA Goddard Space Flight Center, Greenbelt, MD, USA, since 1995 where he has worked on the prelaunch characterization and on-orbit calibration of SeaWiFS, moderate resolution imaging spectroradiometer (MODIS), visible infrared imaging radiometer suite (VIIRS), and now Plankton, Aerosol, Cloud, ocean Ecosystem (PACE) Ocean Color Instrument (OCI). He previously served for seven years as a member of the Cosmic Background Explorer Project FIRAS Analysis Team, NASA Goddard.

Robert H. Estep Jr. received the Bachelor of Aerospace Engineering degree from the Georgia Institute of Technology, Atlanta, Georgia, in 1997, and the Master of Business Administration degree from the University of Houston-Clear Lake, Houston, TX, USA, in 2003.

He joined the National Aeronautics and Space Administration in 1997, where he has supported Agency activities in the Mission Operations Directorate at NASA's Johnson Space Center, the Balloon Program Office at NASA's Wallops Flight Facility, and managing flight instrument projects in the Engineering Technology Directorate and the Flight Projects Directorate at NASA's Goddard Space Flight Center. He was the Instrument Manager for the JWST Micro-Shutter Subsystem that launched in 2022, the SMAP Radiometer which launched in 2015, and Project Manager of the Ocean Color Instrument (OCI) which launched aboard the PACE mission in 2024. Currently he is serving as the Deputy Associate Director of the Planetary Science Projects Division at GSFC.

Eric T. Gorman received the B.S. degree in aerospace engineering from the University of Maryland, College Park, MD, USA, in 2006.

He is currently an Aerospace Systems Engineer and Mission Architect. He has worked multiple flight programs at Goddard Spaceflight Center, Greenbelt, MD, USA, including the Plankton, Aerosol, Cloud, ocean Ecosystem (PACE) mission in which he was the lead engineer for Ocean Color Instrument (OCI) leading the team from proposal through payload delivery. After Goddard, he worked as the director of engineering at Quantum Space and led the technical team to the companies first satellite launch within nine months. He is currently at Northrop Grumman, Baltimore, MD, USA, working on national security space missions.

Samuel Kitchen-McKinley received the bachelor's degree in physics from Clarkson University, Potsdam, NY, USA, in 2005, and the master's and Ph.D. degrees in engineering physics from Embry-Riddle Aeronautical University, Daytona Beach, FL, USA, in 2010 and 2017, respectively.

From 2010 to 2011, he was a Research Associate with the Institute for Human and Machine Cognition, Pensacola, FL, USA. Since 2018, he has been a Senior Research Scientist with Science Systems and Applications Inc., Goddard Space Flight Center, Greenbelt, MD, USA, serving as a Calibration Analyst for Ocean Color Instrument (OCI) and a now as a Data Analyst for GEDI.

David Kubalak received the B.S. and M.S. degrees in optical engineering from the University of Rochester, Rochester, NY, USA, in 1991 and 1993, respectively.

From 1997 to 2005, he was with Orbital Sciences Corporation, Goddard Space Flight Center, Greenbelt, MD, USA. He became a NASA Civil Servant in 2005 and joined the Plankton, Aerosol, Cloud, ocean Ecosystem (PACE)/Ocean Color Instrument (OCI) Team in 2015. His main focus is the alignment, integration, and test of flight optical systems.

Shihyan Lee received the B.S. degree in atmospheric science from Taiwan University, Taipei, Taiwan, in 1995, the master's degree in environmental studies from Boston University, Boston, MA, USA, in 2000, and the Ph.D. degree in satellite remote sensing from the CUNY Hunter College, New York, NY, USA, in 2010.

He is a calibration scientist at the NASA Ocean Ecology Laboratory, working on the calibration and characterization of satellite-based Earth observing sensors.

Charles McClain received the bachelor's degree in physics with a minor in mathematics from the William Jewell College, Liberty, MO, USA, in 1970, and the Ph.D. degree in oceanography from North Carolina State University, Raleigh, NC, USA, in 1976.

From 1976 to 1978, he was a Post-Doctoral Associate with the National Academy of Science/National Research Council, Naval Research Laboratory, Washington, DC, USA. From 1978 to 2014, he worked at the NASA Goddard Space Flight Center, Greenbelt, MD, USA. He currently serves as an Advisor to the Plankton, Aerosol, Cloud, ocean Ecosystem (PACE) Project Scientist, Dr. Jeremy Werdell and as a Co-Editor of the PACE Technical Memorandum Series.

Jeffrey W. McIntire, photograph and biography not available at the time of publication.

Frederick S. Patt received the B.S. degree in physics from Moravian University, Bethlehem, PA, USA, in 1977.

He has supported scientific satellite projects at the Goddard Space Flight Center for over 45 years. Since 1992, he has been supporting the Ocean Color Program with a focus on science data geolocation and calibration, science operations, and data product formats. He is currently the systems engineer and science operations lead for the Plankton, Aerosol, Cloud, ocean Ecosystem (PACE) Science Data Segment. Previously, he supported the Cosmic Background Explorer (COBE) mission and the Flight Dynamics Facility at Goddard.

Zakk Rhodes, photograph and biography not available at the time of publication.

P. Jeremy Werdell received the Bachelor of Arts in biology and environmental science from the University of Virginia, Charlottesville, VA, USA, in 1996, the Master of Science in oceanography from the University of Connecticut, Storrs, CT, USA, in 1998, and the Doctor of Philosophy in oceanography from the University of Maine, Orono, ME, USA, in 2014.

He is currently an Oceanographer with the Ocean Ecology Laboratory, NASA Goddard Space Flight Center (GSFC), Greenbelt, MD, USA. He has worked with the Ocean Ecology Laboratory since 1999, where he currently serves as the Project Scientist for the Plankton, Aerosol, Cloud, ocean Ecosystem (PACE) mission, as well as senior leader of several tasks. His interests extend to the on-orbit calibration of ocean color satellite instruments, the validation of remotely-sensed data products, the collection and analysis of in situ biogeochemical oceanographic measurements, and the assimilation of the above to study how the global ocean and various regional ecosystems are changing with time.